POLITECNICO DI TORINO
Repository ISTITUZIONALE

Characterizing cryogenic chilldown and boil-off: A liquid nitrogen experimental study

Original
Characterizing cryogenic chilldown and boil-off: A liquid nitrogen experimental study / Zumbo, A., Ferrero, A., Masseni, F., Pastrone, D.. - In: APPLIED THERMAL ENGINEERING. - ISSN 1873-5606. - ELETTRONICO. - 310:(2026). [10.1016/j.applthermaleng.2026.133961]

Availability:
This version is available at: 11583/3017747 since: 2026-11-11T09:32:19Z

Publisher:
Elsevier

Published
DOI:10.1016/j.applthermaleng.2026.133961

Terms of use:

This article is made available under terms and conditions as specified in the corresponding bibliographic description in the repository

Publisher copyright

(Article begins on next page)

19 November 2026

Applied Thermal Engineering 310 (2026) 133961

Contents lists available at ScienceDirect

Applied Thermal Engineering

journal homepage: www.elsevier.com/locate/ate

Research Paper

Characterizing cryogenic chilldown and boil-off: A liquid nitrogen experimental study

Alessandra Zumbo *, Andrea Ferrero [a], Filippo Masseni [a], Dario Pastrone [a]

[a] Politecnico di Torino, Corso Duca degli Abruzzi 24, Turin, 10129, Italy

ARTICLE INFO

Keywords:
Cryogenics
Chilldown
Boil-off
Liquid nitrogen
Film boiling

ABSTRACT

Cryogenic chilldown and boil-off directly impact the efficiency, safety and operational margins of any system that handles cryogenic fluids, including propulsion, storage and transfer applications. These processes arise from the interaction between wall heat transfer, boiling regimes, and vapor-space dynamics, and are strongly influenced by geometry, initial thermal conditions, and operating procedures. As a result, well-resolved experimental data remain essential for the development and validation of transient two-phase models. This work presents an experimental investigation of liquid nitrogen chilldown and boil-off in a small-scale test facility composed of two cryogenic vessels, a feed tank and a return tank, connected by a horizontal transfer line. The setup is instrumented to measure temperature evolution, pressure and liquid levels, under controlled valve operations. Wall heat fluxes and mass flow rates are derived from these measurements through energy and mass balances. The influence of initial thermal conditions is examined by comparing chilldown into a pre-cooled transfer line with that of an ambient-temperature configuration under unpressurized flow. To assess the role of the driving mechanism, both unpressurized and pressurized flow transfer conditions are then considered for an ambient temperature transfer line and return tank. Boil-off behavior in the feed tank is characterized at different liquid fill levels and further investigated through controlled heating using an immersed electrical heater. A quantitative mass and energy balance framework is used to reduce the measurements to transfer efficiency, thermodynamic minimum chilldown demand, residual losses, and closed tank energy contributions. The results demonstrate that while pressure-driven transfer shortens the time by more than an order of magnitude at the expense of liquid retention, pre-cooling increases the transfer efficiency and reduces wall enthalpy demand by approximately a factor of three. Over the examined fill level range, sensible heating of the liquid dominates the closed tank energy budget for boil-off, providing a quantitative basis for evaluating the effect of liquid inventory on subsequent thermal evolution and hold-time. These findings quantify the trade-off between transfer speed and cryogen consumption and provide an experimentally supported basis for selecting chilldown strategies under different time and inventory constraints.

1. Introduction

Cryogenic fluid storage and transfer involve thermofluid phenomena governed by strong thermal gradients, phase change and multiphase flow instabilities. During chilldown, the large temperature difference between the incoming cryogenic fluid and the system walls results in complex boiling regimes, rapid pressure fluctuations and significant fluid losses. Once thermal equilibrium is reached, unavoidable heat leak from ambient drives continuous evaporation and boil-off losses that accumulate during the storage period. Both chilldown and boil-off directly govern system efficiency and operational stability: inadequate chilldown results in prolonged cooldown times and increased fluid losses, while underestimating boil-off rates leads to pressure buildup and premature venting.

These challenges arise across a variety of technologies and industrial sectors [1–3]. In the aerospace sector, cryogenic propellants such as liquid hydrogen and liquid oxygen are routinely used in launch vehicles, upper-stage propulsion systems, and emerging in-orbit refueling architectures [4–7], where chilldown efficiency and boil-off losses directly affect mission margins [8]. In the developing hydrogen economy, cryogenic storage is being investigated for long-duration transportation and stationary energy storage applications [9]. Similarly, in sustainable aviation, liquid hydrogen is being considered a promising alternative fuel due to its high gravimetric energy density and potential to eliminate in-flight CO_2 emissions and reduce NO_x emissions [10–12]. Additional industrial applications include liquefied natural gas (LNG) transport, superconducting cooling systems,

* Corresponding author.
E-mail address: alessandra.zumbo@polito.it (A. Zumbo).

https://doi.org/10.1016/j.applthermaleng.2026.133961
Received 19 June 2026; Received in revised form 18 October 2026; Accepted 28 October 2026
1359-4311/© 2026 The Authors. Published by Elsevier Ltd. This is an open access article under the CC BY license (http://creativecommons.org/licenses/by/4.0/).

Nomenclature

Roman symbols

A	cross-sectional area $[m^2]$
c_p	specific heat capacity at constant pressure $\left[\frac{J}{kg\ K}\right]$
c_v	specific heat capacity at constant volume $\left[\frac{J}{kg\ K}\right]$
c_w	specific heat capacity of the walls $\left[\frac{J}{kg\ K}\right]$
D	diameter [m]
f	energy fraction [–]
Fo	Fourier number [–]
h_{fg}	latent heat of vaporization $\left[\frac{J}{kg}\right]$
H	liquid level [m]
k	thermal conductivity $\left[\frac{W}{m\ K}\right]$
K	coverage factor
L	length [m]
$\dot{m}$	mass flow rat $\left[\frac{kg}{s}\right]$
m	mass $[kg]$
$\hat{m}$	non dimensionalized mass [–]
p	pressure [bar]
P	electrical power [W]
q	wall heat flux $\left[\frac{W}{m^2}\right]$
q^*_w	wall stored energy rate per unit area $\left[\frac{W}{m^2}\right]$
s	wall thickness [m]
T	temperature [K]
t	time [s]
$\hat{t}$	non dimensionalized time [–]
u_{rew}	rewetting-front velocity $\left[\frac{m}{s}\right]$
u	internal energy $\left[\frac{J}{kg}\right]$
v	specific volume $\left[\frac{m^3}{kg}\right]$
V	volume $[m^3]$
x	quality [–]

Greek symbols

α	thermal diffusivity $\left[\frac{m^2}{s}\right]$
β	thermal expansion coefficient $[K^{-1}]$
ρ	density $\left[\frac{kg}{m^3}\right]$
Γ	differential energy-balance closure ratio [–]
Δ	difference between two experiments [–]
η	integrated transfer efficiency [–]
Θ	Non dimensional temperature [–]
Π_t	transfer-to-cooling time ratio [–]
σ_{max}	maximum specific liquid requirement [–]
τ_d	diffusion time [s]

Subscripts

amb	ambient
cool	cooling
dewar	dewar
evap	evaporated
ext	external
f, feed	feed tank
h	heater
i	internal
ideal	ideal
l, liq	liquid phase
lat	latent
line	transfer line
m	mean
quench	quenching
r, ret	return tank
ref	reference
rew	rewetting
sat	saturation
sup	superheat
theo	theoretical
tot	total
tr	transfer
v, vapor	vapor phase
w	wall
0	initial

Abbreviations

BO	natural boil-off
BOG	boil-off gas
C	closed
CHF	critical heat flux
CD	chilldown
CO_2	carbon dioxide
DAQ	data acquisition
DP#	differential pressure sensor #
EH1	immersed electrical heater
FBO	forced boil-off
LFP	leidenfrost point
LN_2	liquid nitrogen
LT#	liquid level #
MLI	multi-layer insulation
NO_x	nitrogen oxide
NRV#	non return valve #
O	open
OLS	ordinary least squares
PI#	analog pressure gauge #
PSV#	pressure-release safety valve #
PT1	absolute pressure sensor
RTD	resistance temperature detector
RV#	return valve #
T#	temperature sensor #
V#	valve #

medical cryopreservation, and large-scale scientific facilities requiring cryogenic refrigeration [13–15].

Because of this broad technological relevance, cryogenic chilldown and boil-off phenomena have been studied extensively over the past decades. Work in the space-exploration context has primarily addressed long-term cryogen storage and tank self-pressurization [16–18], propellant dynamics and sloshing [19–21], and materials for liquid hydrogen containment [22]. These studies established the dominant role of ambient heat ingress on pressure buildup and evaporative loss but addressed large flight-weight tanks rather than the transient two-phase phenomena that govern fill and chilldown operations. A parallel line of research on transfer-line chilldown has produced progressively more systematic

datasets and correlations. Parametric investigations by Darr et al. [23,24] characterized the effects of mass flux, inlet subcooling, equilibrium quality, and flow direction on the full Liquid Nitrogen (LN_2) boiling curve across nine flow orientations. Jin et al. [25] conducted horizontal LN_2 pipe chilldown experiments at low mass fluxes, showing that critical heat flux in horizontal flow exceeds that in vertical configurations under these conditions. Hartwig et al. [26] reported chilldown data for liquid oxygen and liquid methane on 2.54 cm and 11.43 cm diameter horizontal lines and identified persistent thermal stratification, highlighting the breakdown of existing correlations outside the conditions for which they were fitted. Narayanan et al. [27] developed a closed loop chilldown test section, enabling controlled initial wall temperatures and well-characterized parasitic losses. More recently, Kim et al. [28] conducted steady-state heated-tube LN_2 flow boiling experiments in horizontal configuration with high-speed flow visualization, providing heat transfer coefficient data across a wide range of mass velocities and confirming the persistence of nucleate boiling within annular flow at high heat flux. Tank-level boil-off has also received sustained attention, though mostly at industrial or aerospace scales. Self-pressurization and stratification in large liquid hydrogen tanks have been investigated experimentally at NASA [17,18,29] and modeled with progressively higher fidelity. At intermediate scale, Perez et al. [30] conducted LN_2 boil-off measurements in a purpose-built 6.7 L cryogenic cell at varying heat fluxes, pressures, and initial liquid volume fractions and showed that thermal stratification in the vapor phase plays a decisive role in setting the boil-off gas (BOG) rate. Fill-level effects on BOG have been investigated numerically and experimentally for C-type large ship tanks using LN_2 as a simulant [31], confirming that the instantaneous wetted wall area and vapor-space geometry govern the transient BOG rate more strongly than total heat input alone.

Despite these contributions, most experimental cryogenic studies investigate components in isolation rather than as an integrated system. Transfer-line chilldown experiments, such as those by Darr et al. [23,24], Jin et al. [25], Hartwig et al. [26], and Narayanan et al. [27], generally consider a single instrumented pipe operated under prescribed inlet conditions, without accounting for the interaction between the supply and receiving tanks. Similarly, studies on large-scale storage vessels [16–18] typically examine the boil-off behavior of a single tank under quasi-steady heat ingress. Taken together, these studies explore a wide variety of working conditions and rig designs, however, to the authors' knowledge, no experimental campaign has been documented in which cryogenic filling and boil-off are investigated on a single coupled two-reservoir facility, with the initial thermal state of the transfer path and the driving mechanism varied independently. Table 1 summarizes representative experimental studies on cryogenic chilldown, filling, self-pressurization and boil-off, grouped by test-article type and phenomena investigated. The present work is included for comparison to highlight the range of operating conditions and phenomena covered by the experimental facility.

The facility used in the present study was originally designed by De Salve and Panella [35,37] to enable coupled two-tank experiments. However, the experiments reported at its commissioning focused on the chilldown of the feed tank and served primarily to demonstrate that the facility functioned as intended. A subsequent work in the same facility [36] extended the campaign to transfer and boil-off operations, but its emphasis was on the experimental procedure and its relevance to aviation applications. The electrical heater installed in the feed tank was not used, and the analysis remained largely descriptive. The present study advances the analysis from a descriptive characterization to a quantitative, system level assessment of the chilldown, transfer and storage process. To achieve this, simultaneous measurements of liquid level, pressure and wall temperature are acquired in both tanks, allowing the system to be treated as two coupled control volumes. Liquid nitrogen is here used as a safe and practical surrogate for cryogenic propellants. The extension of the experimental trends and methodology to other cryogenic fluids is discussed in Section 5.1. The primary objective is to examine how the operating conditions of a coupled two-reservoir cryogenic facility influence its system-level thermal-fluid performance, with particular emphasis on the trade-offs between different transfer and storage strategies. From an operational perspective, these objectives may not be always aligned, and the trade-off depends on the specific requirements and application. The experimental campaign addresses these trade-offs in sequence. First, the effect of different initial thermal condition is isolated by comparing chilldown and transfer into a partially pre-cooled receiving hardware with an ambient-temperature reference under otherwise identical driving conditions. Then, the effect of a higher driving pressure on the cooling time and cryogen consumption is compared to a reference run with an identical initial thermal state. The subsequent analysis investigates how different fill levels influence the thermodynamic behavior of the tank for natural boil-off. The experimental campaign is further extended through the first experimental characterization of forced boil-off in this facility, enabled by the previously unused immersed electrical heater. A differential energy balance between a matched natural/forced pair is utilized to separate the heater contribution from the ambient heat leak. The measurements are analyzed within a common framework that combines transfer efficiency, chilldown efficiency, transfer-to-cooling timescale ratio, and closed-tank first-law partition, allowing the three trade-offs to be assessed using a consistent set of metrics.

2. Test facility and instrumentation

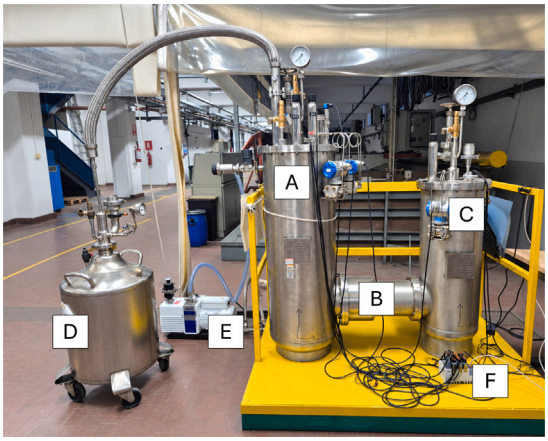
The cryogenic test facility shown in Fig. 1(a) comprises three main components: a feed box, a horizontal transfer section and a return box, connected in series, all of which contain sensors and valves for monitoring and controlling the operating conditions. A schematic is presented in Fig. 1(b). Each cold box consists of two concentric stainless steel vessels separated by an annular vacuum chamber, achieving thermal insulation through a combination of high vacuum and multi-layer insulation (MLI). This allows for detailed investigation of the chilldown phase and two-phase flow in cryogenic systems. The facility enables experiments on LN_2 transfer between tanks, chilldown transients, boil-off phenomena, and heat transfer during flow with subcooled boiling.

2.1. Feed box

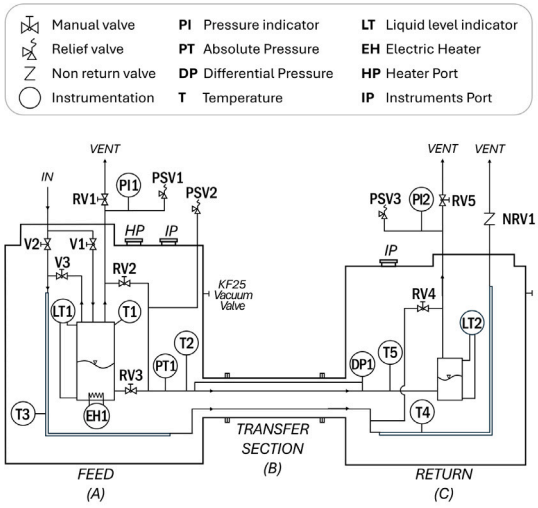
The feed box contains a 15 dm^3 tank that serves as an accumulation tank and phase separator, made from ASTM A312 TP 304/304L stainless steel. The inner tank is a cylindrical vessel with an outer diameter of 168.3 mm, a wall thickness of 3.4 mm, a cylindrical height of 550 mm, and two pseudo-elliptical heads of 168.3 mm diameter, 3 mm thickness, and 60 mm height. Five layers of aluminized Mylar are wrapped around the inner tank to reduce radiative heat input. The tank relative pressure can be regulated from 0 to 9 bar g, providing a wide range of inlet conditions for the transfer section; the feed can be pure liquid, pure vapor, or a two-phase mixture. An immersed electrical heater (48 V, 110 W) allows controlled evaporation of the cryogenic liquid to increase tank pressure. The thermal shield of the feed box is a cylindrical copper shell of 300 mm outer diameter, 0.6 mm wall thickness, and 700 mm height, wound with a gas-cooled helical coil. The coil is a copper pipe of 14 mm outer diameter and 1 mm wall thickness, with a total length of 16 m. Thirty layers of aluminized Mylar are wrapped around the shield, intercepting the bulk of the ambient radiation load before it reaches the cold inner vessel. A separate gas inlet on the feed box allows cold boil-off of gaseous nitrogen to be routed through V1 or V2 valves into the thermal shield coil. If RV1 and shield valve V3 are opened simultaneously, the two paths operate in parallel: RV1 vents directly to atmosphere through a short, large-diameter line, while V3 routes gas through the 16 m helical coil wound around the thermal shield before exhausting (see Fig. 2). The

Table 1
Positioning of the present work against representative experimental studies, grouped by experimental setup family.

Study	Year	Fluid	Experimental setup	Scale	Phenomena	Key focus
Transfer-line studies						
Darr et al. [23,24]	2016	LN_2	Straight SS304 tube	Ø 12.7 mm × 0.55 m	Chilldown	Boiling curve dependence on mass flux
Jin et al. [25]	2016	LN_2	Straight SS304 tube	Ø 12.7 mm × 7 m	Chilldown	Critical heat flux exceeds values at low horizontal mass flux
Hartwig et al. [26]	2022	LOX, LCH_4	Straight SS304 tube	Ø 25.4 and 114.3 mm	Chilldown	Thermal stratification
Narayanan et al. [27]	2024	N_2	closed loop test section	Ø 9.5 mm × 0.6 m	Chilldown	Isolation of initial wall temperature and parasitic losses
S. Kim et al. [28]	2024	LN_2	Steady-state heated tube	Ø 8.5 mm × 0.68 m	Flow-boiling	Heat transfer coefficient across different mass flux
Tank chilldown or filling						
Y. Kim et al. [32]	2016	CF_4	Two-tank rig	Supply 6.0 L, Receiver 5.2 L	No-vent fill	Isolated NVF parameters; non-dimensional map
Xia et al. [33]	2023	LN_2	Single horizontal tank	60 m^3	Chilldown	Cool-down transient and wall thermal stress
Tank boil-off/self-pressurization						
Hopkins & Chronic [16]	1973	LOX, LH_2	Flight-weight tank	6.4 m^3	Boil-off	Long-term storage system
Hasan et al. [17]	1991	LH_2	Flight-weight tank	4.89 m^3	Self-pressurization	Behavior under low wall heat flux
Seo et al. [34]	2010	LN_2	Single insulated tank	6.75 L	Self-pressurization	Effect of fill fraction and heat leak on pressure
Perez et al. [30]	2021	LN_2	Purpose-built dewar	6.73 L	Boil-off	Effect of fill fraction on BOG
Jeon et al. [31]	2022	LN_2	C-type ship tank	0.5 m^3	Boil-off	Fill-ratio and wetted-area effects on BOG
Integrated two-reservoir facilities						
De Salve & Panella [35]	2010	LN_2	Two tanks + line	Feed 15 L, Return 4.8 L	Chilldown	Facility design and feed tank chilldown
Zumbo et al. [36]	2026	LN_2	Same facility	Feed 15 L, Return 4.8 L	Chilldown, natural boil-off	Procedure-oriented preliminary study
Present work	**2026**	**LN_2**	**Same facility**	**Feed 15 L, Return 4.8 L**	**Chilldown, natural boil-off, forced boil-off**	**Independent variation of initial thermal state and driving pressure; first operation of the immersed heater; efficiency and energy-closure analysis with uncertainty propagation**



(a) Overview of the experimental facility. (A) Feed box; (B) horizontal transfer section; (C) Return box; (D) Liquid nitrogen supply dewar; (E) Vacuum pump; and (F) Data acquisition (DAQ) system.



(b) Only the feed box (A), horizontal transfer section (B), and return box (C) shown in panel (a) are represented. Auxiliary equipment (supply dewar, vacuum pump and DAQ system) is omitted.

Fig. 1. Overview of the cryogenic test facility: (a) Experimental facility and (b) Simplified process and instrumentation diagram of the core of the facility.

substantially higher flow resistance of the coil circuit ensures that the majority of the boil-off exits through RV1, while the smaller fraction entering the shield circuit provides cooling of the vacuum jacket. Valve RV1 connects the feed tank to the vent line. Valve RV2 connects the top of the feed tank through the transfer section to the return tank, enabling vapor-phase transfer, while valve RV3 connects the bottom of the feed tank through the transfer section to the return tank, enabling liquid-phase transfer.

2.2. Transfer section

The current configuration for the transfer section has a length of 400 mm and uses a pipe-in-pipe arrangement: the inner pipe, with an inside diameter of 25.5 mm and an outside diameter of 33.3 mm, carries the cryogenic fluid, while the outer vessel serves as the vacuum envelope. The thermal shield pipe has an inside diameter of 10 mm and

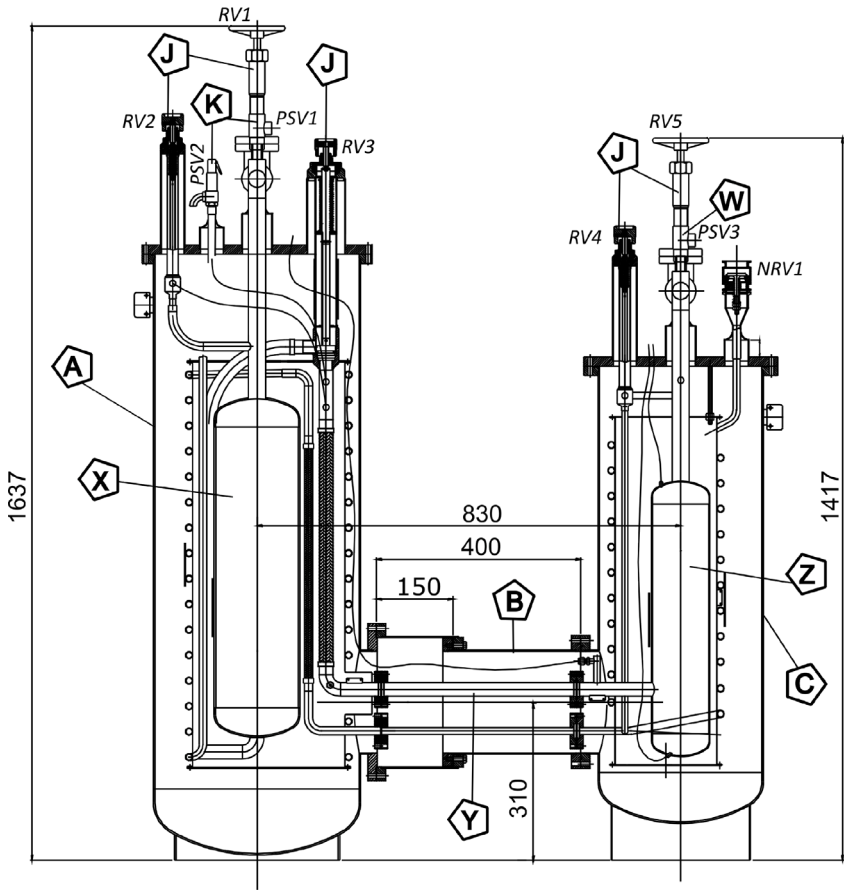


Fig. 2. Cross section of the core of the facility, showing the concentric-vessel arrangement of the feed and return cryostats. (A) Feed box — outer vacuum shell; (X) feed tank — inner LN_2 vessel; (C) Return box — outer vacuum shell; (Z) Return tank — inner LN_2 vessel; (B) horizontal transfer section; (Y) LN2 piping; (J) manual valves; (K) feed tank pressure relief valves; (W) return tank pressure relief valves. The annular gap between each inner vessel and its outer shell contains, from the inner wall outward: 5 layers of aluminized Mylar wrapped on the inner tank, the vacuum jacket, a copper thermal shield wound with a gas-cooled helical coil, and 30 additional layers of aluminized Mylar around the shield. Dimensions in mm.

an outside diameter of 14 mm. The section is modular and can be reconfigured to accommodate small superconducting lines, cryogenic devices operating at liquid nitrogen temperature, or dedicated instrumentation for heat transfer and thermal bridge studies.

2.3. Return box

The return box contains a 4.8 dm^3 cryogenic tank, made from the same steel as the feed tank, which collects the fluid from the transfer section. Five layers of Mylar wrap the inner tank. The thermal shield of the return box is a cylindrical copper shell of 200 mm outer diameter, 0.6 mm wall thickness, and 685 mm height, wound with a gas-cooled helical copper coil of 14 mm outer diameter, 1 mm wall thickness, and 8 m total length. Thirty layers of aluminized Mylar are wrapped around the shield. The tank pressure can be adjusted via vent valves RV4 and RV5 to modify working conditions; RV4 connects the shield line to the top of the return tank, and RV5 connects the exhaust line for gas venting and boil-off evacuation. The fluid collected in the return tank evaporates due to residual heat input and is released to the atmosphere through the vent valve RV5.

2.4. Instrumentation and data acquisition

The process is controlled by the status of the various valves, initial wall temperatures, and gas pressure within the tanks. Five four-wire RTD thermometers (PT 100 IEC 751 class A, in the range 73 K – 323 K) measure the temperatures at the feed tank wall (T1), the transfer section inlet (T2), the thermal shield in the feed and return (T3, T4) and the transfer section outlet (T5). The five channels differ only in their location on the facility and on the wall they instrument; their positions and mounting are summarized in Table 2. Axial coordinates on the transfer line, x, are referred to the feed-tank outlet flange along the flow direction ($L_{\text{line}} = 400$ mm); vertical coordinates, z, are referred to the lower tangent line of the cylindrical shell of the feed or return tank. All five sensors measure the outer wall metal temperature, and sensor uncertainties are reported in Table 3. Sensors are mounted externally on the tank and transfer-line walls via dedicated bracket-and-bolt assemblies designed by the facility manufacturer, ensuring direct metallic contact with the wall. A single wall-mounted RTD was used on each reservoir, consistent with the original facility design of De Salve and Panella, which was developed to investigate the coupled thermal behavior of the feed tank, transfer line, and return tank at the system level rather than to resolve internal temperature distributions. As a result, the current observations do not resolve the axial temperature stratification within the tanks and transfer line. However, the sensors are placed at physically relevant locations for the processes investigated, and the main quantitative analyses in Sections 5 are based on integrated energy balances rather than spatially resolved temperature fields. Two differential pressure transducers (range 0–6 kPa), LT1 and LT2, allow the evaluation of the liquid level in the feed and return cryostats, while the absolute pressure is measured by means of PT1 sensor and the pressure drop in the transfer section by means of the differential pressure sensor DP1. To verify measurement consistency, sensor readings were compared throughout the campaign to the ambient equilibrium state recorded before and after each run. All channels

Table 2
Location of the wall-temperature RTDs. Datums: z from the lower tangent line of the feed (or return)-tank cylindrical shell; x from the transfer section inlet.

Probe label	Measurement	Location	Mounting position
T_1	Temperature of the feed tank reservoir wall	$z_f = 0$ mm	Bottom
T_3	Temperature of the thermal shield of the feed tank	$z_f = 392$ mm	Side
T_4	Temperature of the thermal shield of the return tank	$z_r = 310$ mm	Side
T_2	Temperature of the wall at the transfer-section inlet	$x = 0$ mm	Bottom
T_5	Temperature of the wall at the transfer-section outlet/return tank inlet	$x = 400$ mm	Bottom

Table 3
Baseline measurement uncertainties.

Parameter	Instrument	Range	Tolerance
T1–T5	RTD PT100 IEC 751 Class A	73–323 K	$\pm(0.15 + 0.002 \cdot \lvert T \rvert)$ K
LT1, LT2, DP1	Differential pressure transducer	0–60 mbar	±0.1% F.S.
PT1	Absolute pressure transducer	0–10 bar	±0.2% F.S.

returned to values within the specified uncertainty range, indicating that the measurement chain remained stable throughout the experimental sequence. All data is acquired and processed via an NI compactRIO 9053 equipped with a NI 9216 and NI 9207 boards, controlled by a custom LabView program.

3. Methodology

Each test follows a common preparation sequence. Prior to conducting any experiment, a vacuum environment is established within the thermal shields and vacuum-insulated pipes using a Value VRD16 dual-stage rotary vane vacuum pump (pumping speed 16 m^3/h, ultimate pressure $4 \cdot 10^{-3}$ mbar). The feed tank is then filled with LN_2 from a pressurized supply dewar (capacity ≈ 35 kg). The dewar is equipped with an internal dip tube that draws liquid from the bottom of the vessel; autogenous pressurization due to natural boil-off within the sealed dewar ($p_{dewar} \approx 1.1$ bar) provides the driving force to push liquid upward through the flexible transfer line to the feed tank inlet valve V1, while vapor is simultaneously vented through RV1. Once the target initial state is established, data acquisition is started and the valve sequence specific to each run is executed. Two different test typologies are considered in the present work: chilldown and boil-off. For the chilldown runs, designated CD0-CD3, the valve sequence is specified in Tables 5–9. For boil-off experiments, all vent valves are closed after the feed tank has reached the desired fill level, sealing the system. Runs conducted under ambient heat leak alone are designated BO1-BO3 ($P_{heater} = 0$), while those with the immersed electrical heater active are designated FBO1-FBO2 ($P_{heater} > 0$). The valves and heater state for these runs is given in Table 10.

3.1. Results analysis and performance metrics

The liquid nitrogen mass flow rate in both tanks is calculated using [35]:

$$\dot{m}_{LN_2} = \rho_{l,sat}(T)\, A(t) \frac{dH}{dt} \tag{1}$$

where $\rho_{l,sat}(T)$ is the saturation density of liquid nitrogen evaluated at the measured temperature, $A(t)$ is the cross-sectional area of the tanks as the liquid level changes, and $\frac{dH}{dt}$ is the derivative of the liquid level, which is proportional to the liquid flow rate across the transfer section.

To quantify how much of the liquid nitrogen leaving the feed tank is successfully delivered as liquid to the return tank, a mass-integrated transfer efficiency is defined as

$$\eta = \frac{\Delta m_r}{\Delta m_f} = \frac{\rho_l[V_{l,r}(t_f) - V_{l,r}(t_0)]}{\rho_l[V_{l,f}(t_0) - V_{l,f}(t_f)]} \tag{2}$$

where $V_{l,f}$ and $V_{l,r}$ are the liquid volumes in the feed and return tanks computed from the differential-pressure level measurements and the tank geometry, and $[t_0, t_f]$ spans the transfer phase of the run. The complement $1-\eta$ represents the fraction of the transferred mass lost as vapor, vented from the return tank, comprising the liquid evaporated to chill down the transfer line and the return tank walls plus ambient heat in-leak during transit. This integrated definition is preferred over a ratio of peak instantaneous mass flow rates because the peaks of $\dot{m}_f$ and $\dot{m}_r$ occur at different instants and reflect different physical states of the facility. The measured efficiency η is compared with the corresponding theoretical value in Section 5.1, where the different tests are assessed in terms of liquid delivery and competing requirements of chilldown time, cryogen utilization and liquid retention. The resulting metrics are therefore used to separate the thermodynamic demand associated with cooling the receiving hardware from additional losses caused by the transfer procedure.

The second part of the analysis addresses the thermal response of the feed tank wall. The starting point is the radial energy balance on the cylindrical wall [35]:

$$\rho_w(T)\, c_w(T)\, s\, D_m \frac{dT_w}{dt} = q_e\, D_e - q_i\, D_i \tag{3}$$

where $\rho_w(T)$ and $c_w(T)$ are the temperature-dependent wall density and specific heat of AISI 304, s is the wall thickness, D_m, D_e and D_i are the mean, external and internal diameters, q_e is the heat flux from the thermal shield to the outer wall, and q_i is the heat flux from the inner wall to the fluid. The wall density $\rho_w(T)$ is computed from [38]:

$$\rho(T) = \rho_{300} \exp\left(- \int_{T_0}^{T} 3\, \beta(T)\, dT \right) \tag{4}$$

with the temperature-dependent thermal expansion coefficient $\beta(T)$ of AISI 304 taken from [38] and ρ_{300} the wall density at the reference temperature $T_0 = 300$ K. The specific heat $c_w(T)$ is evaluated using the empirical logarithmic correlation $c_P(T) = 10^k$, in which the exponent k is expressed as a polynomial function of $\log_{10}(T)$ with coefficients derived from NIST data [38].

Chilldown regime. During chilldown, the rate of heat loss from the wall to the cold nitrogen is orders of magnitude higher than the heat leaks from the outside through the vacuum jacket, thus, external heat leak is negligible ($q_e D_e \ll q_i D_i$) and Eq. (3) reduces to

$$q_i = -\rho_w(T)\, c_w(T)\, s \frac{D_m}{D_i} \frac{dT_w}{dt} \tag{5}$$

During chilldown $\frac{dT_w}{dt} < 0$, so $q_i > 0$. The time offset between the peak cooling rates $|dT/dt|$ at sensors T2 and T5 provides a direct estimate of the rewetting-front velocity along the transfer section:

$$u_{rew} = \frac{L_{line}}{t_{quench,5} - t_{quench,2}} \tag{6}$$

where t_{quench} denotes the instant at which $|dT/dt|$ is maximum for each sensor.

Table 4
Summary of chilldown runs. $T_i,0$: initial temperature at RTD sensor i; $p_{f,0}$: initial feed-tank pressure; Δm_f and Δm_r: mass leaving feed and accumulated in return; $\eta = \Delta m_r/\Delta m_f$: transfer efficiency; ΔT_i: temperature drop at sensor i during experiment; $\Delta t_{\mathrm{drop},i}$: time required to reach the temperature drop at sensor i from experiment start.

Run	Initial conditions				Transfer flow metrics			Outcome metrics					
	$T_{1,0}$ [K]	$T_{2,0}$ [K]	$T_{5,0}$ [K]	$p_{f,0}$ [bar]	Δm_f [kg]	Δm_r [kg]	η [–]	ΔT_1 [K]	ΔT_2 [K]	ΔT_5 [K]	$\Delta t_{\mathrm{drop},1}$ [s]	$\Delta t_{\mathrm{drop},2}$ [s]	$\Delta t_{\mathrm{drop},5}$ [s]
CD0	291.5	–[a]	–[a]	1.0	–[a]	–[a]	–[a]	214.4	–[a]	–[a]	1050	–[a]	–[a]
CD1-fl[b]	99.6	151.1	143.4	1.0	–[a]	–[a]	–[a]	21.1	–[a]	–[a]	890	–[a]	–[a]
CD1-tr[b]	78.5	171.9	161.3	1.0	4.62	2.99	0.65	–[c]	91.2	66.5	–[c]	604	1030
CD2	79.3	259.6	291.3	1.0	6.48	3.60	0.55	–[c]	179.1	188	–[c]	1160	1400
CD3	80.2	260.9	289.5	2.0	8.42	0.88	0.10	–[c]	180.3	181.6	–[c]	750	1081

[a] Initial value irrelevant to the physics under study: valve RV3 remains closed throughout experiment (chilldown of feed tank only).
[b] For CD1, the reported initial conditions are split for the two distinct phases of experiment: *CD1-fl* is the start of the filling phase (t = 0, Sec 4.2) and *CD1-tr* is the subsequent transfer phase (t ≥ 3560 s), which is the reference against which CD2 is compared in Section 4.3.1. The outcome metrics refer to the transfer phase only.
[c] Not applicable, feed tank already filled at test start.

Table 5
Valve states during CD0 experiment phases. 'O' indicates Open and 'C' indicates Closed.

Phase [s]	V1	V2	V3	RV1	RV2	RV3	RV4	RV5
0–50	C	C	O	O	C	C	C	C
50–3000	O	C	O	O	C	C	C	C

Boil-off regime. During boil-off with all vent valves closed, the tank self-pressurizes and the wall temperature rises slowly ($dT_1/dt \sim 10^{-3}$ K/s). In this quasi-steady regime, the left hand side of Eq. (3) represents the wall stored energy rate per unit area, denoted q_w^* to distinguish it from the wall-to-fluid heat flux q_i used in the chilldown analysis:

$$q_w^* \equiv \rho_w(T)\, c_w(T)\, s\, \frac{D_m}{D_i}\, \frac{dT_1}{dt} = q_e \frac{D_e}{D_i} - q_i \tag{7}$$

This quantity represents the rate at which thermal energy accumulates in the tank wall per unit inner surface area.

3.2. Uncertainty analysis

All uncertainties reported in this work are evaluated in accordance with the Guide to the Expression of Uncertainty in Measurement [39]. For each measured and derived quantity, the combined standard uncertainty accounts for both Type B contributions, taken from the manufacturer's specifications, geometric tolerances and property data, and Type A contributions, evaluated statistically from the recorded signals. Table 3 presents the manufacturer instrument tolerances. The combined standard uncertainty u_c of each derived quantity $y = f(x_1, \ldots, x_n)$ is obtained by propagating the standard uncertainties of its inputs through its defining expression, according to the law of propagation of uncertainty. Throughout Section 4, shaded bands and error bars on figures denote the expanded uncertainty ($U = K \cdot u_c$) at the $K = 2$ (≈ 95%) confidence level. The complete methodology is reported in Appendix A.2 along with a summary of the median expanded uncertainty of each plotted quantity for every run (Table 16). Where specific values are discussed in the text, such as the characteristic points of the boiling curve or scalar results, their $K = 2$ uncertainty is given alongside.

4. Results

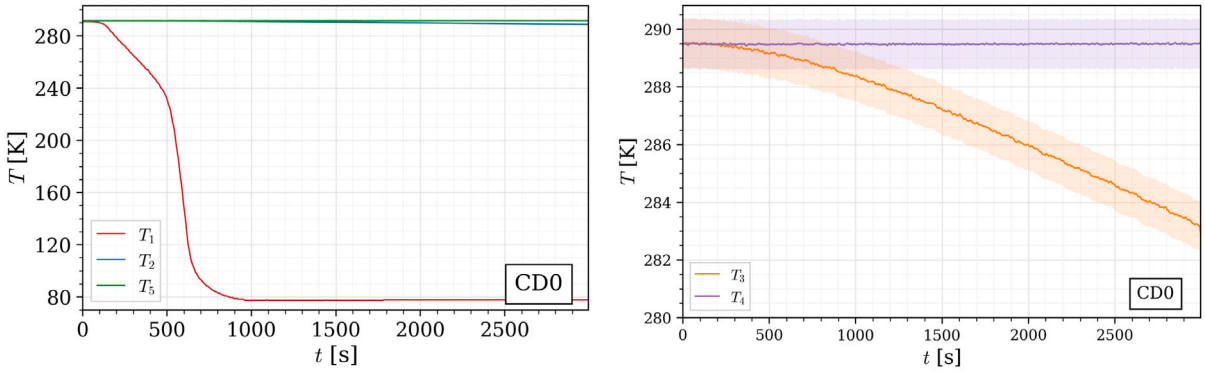
The experimental campaign consists of two primary types of tests: chilldown and transfer experiments, in which liquid nitrogen is introduced into a warm or partially pre-cooled system, and boil-off experiments, which monitor the evolution of a liquid nitrogen mass in the feed tank under ambient heat ingress or controlled electrical heating. A summary of the tests is presented in Tables 4 and 11.

4.1. Validation run: feed tank chilldown

The first phase of the experimental campaign validates previously conducted tests [35]. Experiment CD0 serves as an instrumentation and setup validation experiment, reproducing the feed tank chilldown and filling procedure reported by De Salve and Panella [35]. Liquid nitrogen is transferred from a supply dewar ($p_{\mathrm{dewar}} \approx 1.1$ bar) into the feed tank through valve V1, with vapor vented to the atmosphere via RV1, the valve configuration for this experiment is shown in Table 5. No flow occurs in the transfer section connecting the feed box to the return box throughout the transient, since RV3 remains closed throughout the test: the differential pressure DP1 oscillates around its offset value of 0.088 kPa, and the feed tank pressure PT1 remains essentially constant at ambient pressure. The wall temperature T1, shown in Fig. 3(a), exhibits the characteristic cooling curve associated with the successive heat transfer regimes that develop as liquid nitrogen contacts a warm cryogenic vessel. An initial phase of single-phase gas convection is followed by a quenching transient in which stable and unstable film boiling coexist with non-negligible axial conduction along the tank wall. This gives way to a final regime dominated by transient nucleate pool boiling as the wall temperature approaches the saturation temperature of LN_2. Between $t \approx 150$ s and $t \approx 500$ s, the wall temperature decreases at a nearly constant rate of $dT_1/dt \approx -0.149$ K/s, indicating an approximately linear cooling process consistent with a quasi-steady heat flux at the wall surface. From $t \approx 500$ s onward, the feed tank temperature shows a rapid asymptotic decay to T_{sat} characteristic of transient nucleate pool boiling, with $|dT_1/dt|$ decreasing monotonically as the wall superheat is consumed. The quasi-steady cooling rate $dT_1/dt \approx -0.149$ K/s measured between 150 s and 500 s demonstrates an acceptable agreement with values reported in the same facility [35], with variations on the order of 10%.

Since the transfer line valve RV3 remains closed for the whole duration of the test, the temperature inside the return box T5 remains constant at 290 ± 0.8 K. The inlet transfer section temperature T2 decreases from 290 ± 0.8 K to approximately 288 ± 0.8 K over approximately 3000 s, as shown in Fig. 3(a). This moderate cooling is attributed primarily to axial conduction along the flexible connections linking the feed tank to the transfer section outlet flange, rather than to any direct contact with liquid nitrogen.

The progressive cooling of the feed tank wall drives a corresponding cooling of the surrounding thermal shield through thermal radiation. Fig. 3(b) shows the time evolution of the shield temperatures T3 and T4. During the filling transient, the copper shield temperature T3 decreases from an initial value of 289.5 ± 0.8 K to approximately 283.3 ± 0.8 K. This cooling is primarily driven by radiative exchange between the shield and the inner tank wall, which is rapidly cooling toward the LN_2 saturation temperature, but is partly attributable to the cold nitrogen gas circulating in the thermal shield coil through valve V3, open during the test. The return-side shield sensor T4 remains flat



(a) Wall feed tank temperature (T1) and inlet/outlet transfer section temperatures (T2 and T5). Uncertainty bands (95% confidence level) are plotted but not visible at this scale

(b) Thermal shield temperatures in the feed (T3) and return (T4) box.

Fig. 3. Temperatures for chilldown of feed tank only, experiment CD0.

Table 6
Comparison of geometry, material properties, and initial/boundary conditions between the present CD0 experiment and Xia et al. [33].

Parameter	Present Work (CD0)	Xia et al. (2023) [33]
Geometry & Material		
Tank orientation	Vertical	Horizontal
Tank volume	15 L (feed tank)	60 m^3
Inner diameter	161.5 mm	2.6 m
Inner wall material	SS304	S30408 (304 in ASTM standard)
Wall thickness (s)	3.4 mm	15.7 mm
Insulation	MLI+ vacuum insulation	Vacuum powder (pearlite)
Initial & Boundary Conditions		
Working fluid	Liquid Nitrogen (LN_2)	Liquid Nitrogen (LN_2)
Initial wall temperature	292 K	280 K
Inlet fluid temperature	77 K	77 K
Volumetric flow rate	0.4 L/min (mean delivered)	35 and 43 L/min

at 289.5 ± 0.8 K since the transfer valve remains closed throughout the experiment and no LN_2 passes in the return tank.

The quench trajectory shown in Fig. 4b displays the regime sequence described above, progressing from high to low temperature, shown on the left in 4a. The three-stage cooling behavior is consistent with the tank chilldown phenomenology reported by Xia et al. [33]: an initial single-phase vapor convection and film-boiling regime at high wall superheat, followed by a minimum heat flux at the Leidenfrost point (LFP, $T_l \approx 260 \pm 0.7$ K, $\Delta T_{sup} \approx 183$ K), transition boiling with increasing heat flux, and the critical heat flux (CHF, $T_l \approx 165 \pm 0.5$ K, $\Delta T_{sup} \approx 88$ K, $|q_i| = 11941 \pm 531$ W/m^2). Below the CHF, nucleate boiling dominates and the wall temperature drops rapidly toward T_{sat}.

For a 60 m^3 horizontal LN_2 storage vessel, Xia et al. [33] applied Burggraf's inverse heat conduction method to outer-wall thermocouple measurements [40] and reported a peak heat flux of approximately 20−25 kW/m^2 at the tank bottom at the onset of the boiling-dominated stage, compared with approximately 12 kW/m^2 measured in the current study. The significant differences between the two configurations should be considered when comparing these values. The present study involves a small-scale vertical cylinder while Xia et al. investigated a large-scale horizontal cylinder. A comparison of the two systems in terms of geometry, material properties and operating conditions is given in Table 6.

To verify that the thin-shell form of Eq. (5) is appropriate for the present study, the wall flux was independently reconstructed from the same temperature history using the exact cylindrical inverse-conduction solution of Burggraf [40], in the three-term formulation adopted by Xia et al. [33] for a chilldown problem. Eq. (5) corresponds algebraically with the first term of that solution, while the other terms involve the second and third time derivatives of the outer wall temperature and account for the finite radial diffusion time across the wall. The wall Fourier number can be used to determine their relative importance.

$$\mathrm{Fo}_s = \frac{\alpha_w t}{s^2} = \frac{t}{\tau_d} \tag{8}$$

where t is the timescale of the outer-wall temperature transient around the peak-flux condition and $\tau_d = s^2/\alpha_w$ is the wall diffusion time. For the present experiment, $\mathrm{Fo}_s \approx 100$, while the corresponding value for the Xia et al. configuration is approximately $\mathrm{Fo}_s \approx 5$. The larger Fourier number for the present experiment reflects the shorter diffusion time of the thinner wall relative to the timescale of the observed transient.

The three-term Burggraf reconstruction for the experiment CD0 is plotted in Fig. 4b and provides a direct check of the relevance of the higher-order terms. The first-term approximation of Eq. (5) and the full Burggraf reconstruction agree to within approximately ±0.3% at the peak heat flux, remaining well inside the K = 2 uncertainty band of Eq. (5). This suggests that the second- and third-derivative contributions are negligible at the wall thickness and temporal resolution of the present experiment. Moreover, inclusion of these terms introduces increasing sensitivity to measurement noise because numerical differentiation amplifies noise at each successive derivative order, as documented for cryogenic inverse-conduction measurements [23]. The first-term approximation is therefore adopted for the present study.

4.2. Feed tank chilldown and filling of pre-cooled tank with LN_2

Run CD1 extends the CD0 validation by characterizing the chilldown of the transfer section and return tank under unpressurized flow, with the feed tank at atmospheric pressure. Unlike CD2 and CD3, the transfer line and return box are initially in a partially pre-cooled state ($T_2 = 150 \pm 0.5$ K, $T_5 = 143 \pm 0.5$ K) and the feed tank itself starts at

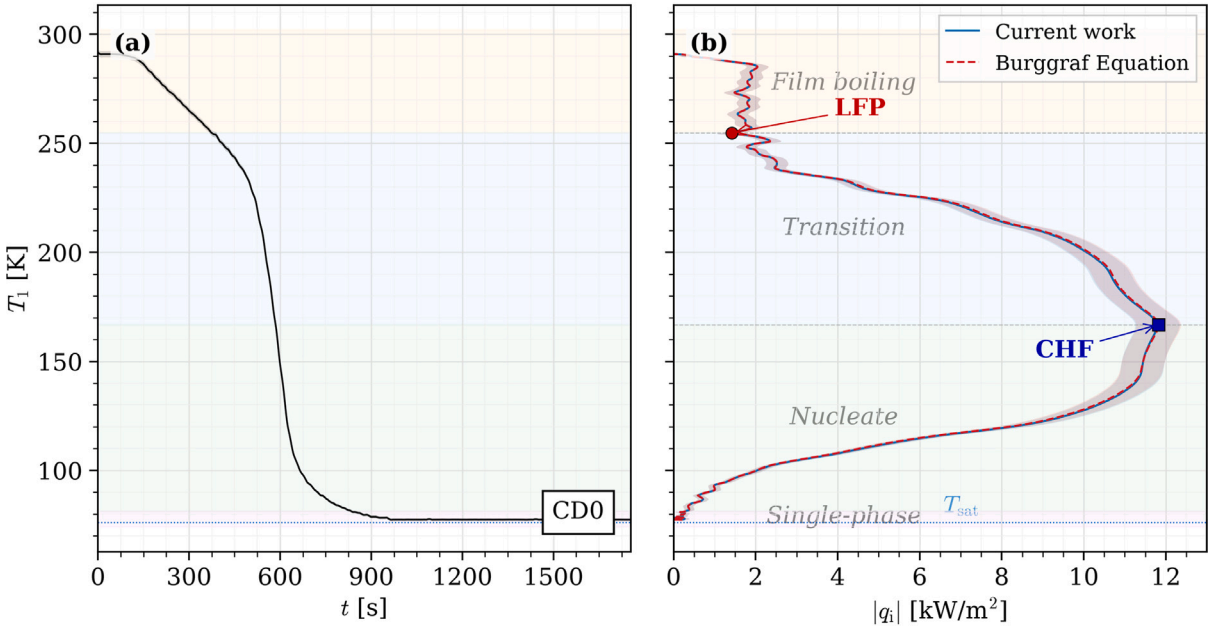


Fig. 4. CD0 boiling curve at the feed tank wall. (a) Wall temperature T_1 vs time. (b) Heat flux curve: comparison of lumped model against Burggraf solution. The shaded bands curves represent the corresponding uncertainty bounds, with peak values specified in text.

Table 7
Valve states during CD1 experiment phases. 'O' indicates Open and 'C' indicates Closed.

Phase [s]	V1	V2	V3	RV1	RV2	RV3	RV4	RV5
0–300	C	C	C	C	C	C	C	C
300–890	O	C	C	O	C	C	C	C
890–3560	C	C	O	O	C	C	C	O
3560–5300	C	C	C	C	C	O	C	O
5300–6000	C	C	C	O	C	C	C	O

$T_1 = 99.6 \pm 0.4$ K. The run is reported as two consecutive phases in Table 4 as CD1-fl and CD1-tr: (i) a filling phase ($0 \leq t \leq 3560$ s), in which the feed tank is loaded with LN_2 from the supply dewar through V1, with the transfer section isolated by RV3; and (ii) a transfer phase ($t \geq 3560$ s), initiated by opening RV3 at $t \approx 3560$, in which the partially pre-cooled feed tank delivers liquid to the return tank through the line. The transfer phase serves as the reference unpressurized experiment against which the ambient-temperature line experiment CD2 is compared in Section 4.3.1, while the filling phase is reported for completeness and to define the pre-transfer thermal state of the line and return tank.

After achieving the required vacuum conditions using the vacuum pump system, the experiment proceeds as follows. Initially, all valves are closed. About 300 s after data acquisition begins, the liquid inlet valve V1 and the feed tank vent RV1 are opened. The temperatures measured by sensors T1, T2, and T5 are shown in Fig. 5(a). Sensor T1 shows a rapid drop from 99.6 ± 0.4 K to 78.5 ± 0.3 K as LN_2 enters the feed tank, caused by heat removal via boiling and conduction from the tank walls. The filling phase (CD1-fl) concludes at approximately 890 s when the feed tank reaches capacity. At this point, fill valve V1 is closed and thermal shield vent V3 is opened, diverting the boil-off gas through the shield coil. As the system sits without active flow, ambient heat gradually warms the transfer line. This causes temperatures T2 and T5 to slowly drift upward from roughly 150 ± 0.5 K and 143 ± 0.5 K at $t = 0$ s to 172 ± 0.6 K and 162 ± 0.6 K by $t \approx 3560$ s. The transfer phase (CD1-tr) begins when RV3 is opened to connect the feed and return tanks; simultaneously, RV1 is closed and RV5 is opened to vent the return tank. As the cold LN_2 flows into the partially pre-cooled transfer section, T2 and T5 register a sharp drop. Section 4.3.1 provides a detailed analysis of this transfer phase and compares it against CD2.

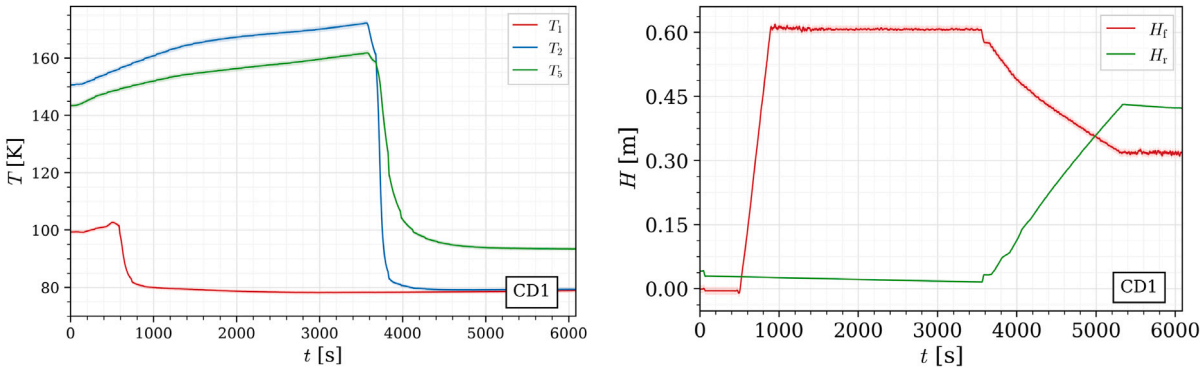
Fig. 5(b) shows the liquid level trends in the tanks. The feed tank begins filling shortly after the valves are opened, with a nearly linear increase until reaching its maximum capacity of 60.61 ± 0.13 cm. The return tank starts filling once valve RV3 is opened ($t \approx 3560$ s), eventually reaching approximately 43.02 ± 0.09 cm ($t \approx 5300$ s) when valve RV3 is closed. When the dewar supply is stopped and no liquid transfer occurs, the level decreases due to boil-off. If vent valves RV1 or RV5 remain open, as in the final phase of this test ($t \geq 5300$ s), this occurs at nearly constant pressure. Fig. 6(a) presents the time evolution of the flow rates. At the beginning of the experiment, the feed tank flow rate peaks sharply at $\dot{m}_f = 0.028 \pm 0.001$ kg/s upon opening valve V1. It then remains approximately constant during filling and drops to zero once the tank is full. When transfer begins, the return tank flow rate rises and stabilizes, while the feed tank flow becomes negative due to liquid depletion. The return tank flow is lower than the initial filling flow, as boiling occurs from its higher initial temperature. The thermal flux resulting from Eq. (5) is represented in Fig. 6(b), where the peak ($q_i = 2.1 \pm 0.09$ kW/m^2) corresponds to the maximum rate of heat removal from the wall during the filling transient.

4.3. Transfer line and return tank chilldown

The following two subsections present the chilldown experiments conducted with the transfer section and return tank initially at ambient temperature. The experiments start with the feed tank already filled. The effect of the initial thermal state is first isolated in Section 4.3.1 by comparing the unpressurized run CD2 against the pre-cooled reference CD1. In runs CD1 and CD2, the feed tank is at atmospheric pressure; the only driving force for the feed-to-return transfer is the hydrostatic head of the LN_2 column in the feed tank. These runs are designated as unpressurized transfers to distinguish them from CD3, presented in Section 4.3.2, in which the feed tank is self-pressurized to 2 bar ($p_{feed} = 2$ bar).

4.3.1. Unpressurized transfer

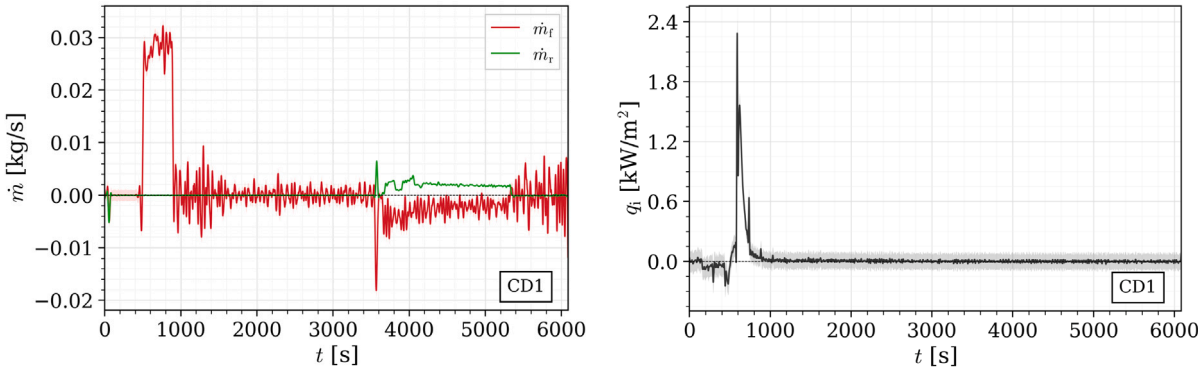
Experiment CD2 was carried out to compare the chilldown of transfer section and return tank at different initial condition. Unlike CD1, previously described, in experiment CD2 the transfer section and return tank were at ambient temperature ($T_2 = 259.6 \pm 0.7$ K, $T_5 = 291.3 \pm$



(a) Wall feed tank temperature (T1) and inlet/outlet transfer section temperatures (T2 and T5)

(b) Feed (H_f) and return (H_r) liquid level history during chilldown

Fig. 5. Temperature and liquid level trends during experiment CD1.



(a) Mass flow rate inside the feed and return tanks

(b) Thermal flux inside the feed tank estimated by Equation 5

Fig. 6. Mass flow rate and thermal flux evolution during experiment CD1.

Table 8
Valve states during CD2 experiment phases. 'O' indicates Open and 'C' indicates Closed.

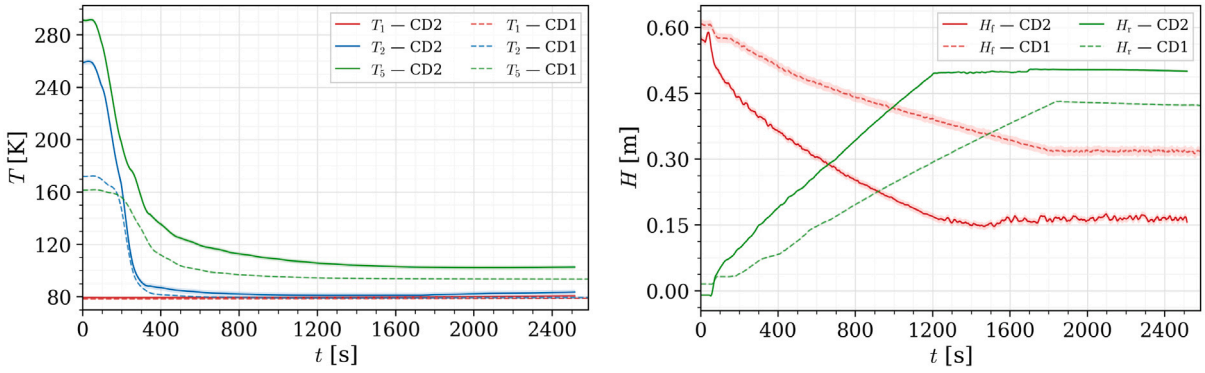
Phase [s]	V1	V2	V3	RV1	RV2	RV3	RV4	RV5
0–50	C	C	C	O	C	C	C	O
50–1230	C	C	C	C	C	O	C	O
1230–2500	C	C	C	C	C	C	C	O

0.8 K), and the filling of return occurred under ambient-temperature conditions. The experiment starts with the feed tank completely filled ($T_1 = 79.3 \pm 0.3$ K), and every curve is plotted against the transfer phase of experiment CD1 (CD1-tr in Table 4), from about 3560 s onward. Prior to opening valve RV3, valve RV5 was opened to vent the return tank, and RV1 was closed, as highlighted in Table 8. Fig. 7(a) shows the temperature trends. While the feed tank wall remains near 79 K, temperatures upstream (T2) and downstream (T5) of the transfer section drop sharply as transfer begins.

In both experimental runs, the temperature readings at the T2 sensor stabilize at a similar baseline of approximately (81 ± 0.4 K for CD1 and 85 ± 0.4 K for CD2), which is maintained by the continuous flow of liquid nitrogen from the supply tank until valve RV3 is closed at around 1230 s, when return tank capacity is reached.

At the downstream sensor T5, wall temperature decreases monotonically over the course of the transfer, but saturation is not reached before the valve is shut. In CD2, T5 reaches approximately 107 ± 0.4 K at valve closure. After closure, no additional liquid is supplied to the transfer line, and the wall temperature continues to decrease more slowly, approaching a plateau in the range of 95–100 K. This post-closure evolution is attributed to the residual fluid evaporating in the transfer line and the subsequent thermal relaxation of the wall toward the surrounding structures. The terminal temperature therefore reflects the extent of chilldown achieved before valve closure rather than a fully developed steady-state condition. The lower terminal temperature observed for the pre-cooled condition (CD1) is consistent with the lower initial wall enthalpy and the resulting greater degree of chilldown achieved within the same transfer window.

While the final states are similar, the distinct thermal trajectories of the pre-cooled (CD1) and ambient-temperature (CD2) runs differ substantially during the initial cooling phase. Specifically, the pipe wall in the ambient run must dissipate roughly 180 K of stored thermal energy, compared to only 90 K in the pre-cooled run. Furthermore, only the ambient case begins with a temperature differential large enough to trigger film boiling. During the ambient-temperature run (CD2), rapid initial boiling creates a continuous layer of vapor that temporarily insulates the pipe wall from the liquid coolant. This behavior aligns with the liquid-core and vapor-film structure detailed in the National Bureau of Standards (NBS) study on cryogenic cooling [41]. This insulating vapor layer maintains an elevated temperature plateau at T5 for the first 150 to 200 s after the valve opens. This phase is characterized by temporary vapor generation and pressure instability, which significantly extends the overall cooling time. Once the temperature difference between the wall and the fluid drops sufficiently, the vapor layer breaks down. The system then shifts into a more efficient heat-transfer phase (nucleate boiling) and rapidly cools to its final saturated state. Conversely, in the pre-cooled run (CD1), the initial temperature difference is already too small to support film boiling. Consequently, the system completely bypasses the prolonged, insulated phase. The temperature at T5 drops steadily and continuously toward its final state from the moment the valve opens. Ultimately, although pre-cooling the system does not affect



(a) Wall feed tank temperature (T1) and inlet/outlet transfer section temperatures (T2 and T5) history

(b) Feed (H_f) and return (H_r) liquid level history during chilldown

Fig. 7. Temperature and liquid level trends comparison during transfer with non pre-cooled (CD2) and pre-cooled (CD1) return tank. Valve RV3 is closed at around $t = 1740$ s for CD1 and $t = 1230$ s for CD2.

its final thermal equilibrium, it influences the heat-transfer mechanisms the system experiences during the cooling process.

Fig. 7(b) shows the evolution of liquid levels in the two tanks. The observed differences between the experiments can be attributed to the thermofluid regimes in the transfer section after valve opening. In the ambient-temperature line (CD2), the inflow of liquid nitrogen triggers intense film boiling, forming a vapor layer that facilitates rapid flow of the inner liquid core through the transfer section [35]. This produces a sharp transient in the flow rate and a faster rise in the liquid level in the return tank. In contrast, in the pre-cooled line (CD1), the system is near cryogenic temperature, and the liquid maintains direct contact with the wall.

Flow rate trends in the feed and return tanks (Fig. 8(a)) further highlight these differences. In the ambient-temperature case, initial mass flow peaks are much higher due to rapid evaporation and vapor expansion within the line. This vapor generation causes transient pressure surges and partial venting, resulting in significant nitrogen losses. Although the return tank fills faster in the hot case, overall transfer efficiency is lower due to increased boil-off. During CD2 the feed-tank outflow peaks at $\dot{m}_f = 0.029 \pm 0.001$ kg/s and the return-tank inflow at $\dot{m}_r = 0.010 \pm 0.001$ kg/s, then decays to a quasi-steady $\dot{m}_f \approx \dot{m}_r \approx 1.5$ g/s sustained over the remainder of the transfer; in CD1, both peaks are roughly three times smaller ($\dot{m}_f = 0.011 \pm 0.001$ kg/s, $\dot{m}_r = 0.003 \pm 0.001$ kg/s) while the quasi-steady tail is comparable to CD2.

Table 4 summarizes the aggregate outcome. Starting with $m_{LN_2} = 8.52$ kg of liquid nitrogen in the feed tank, the ambient-temperature configuration (CD2) discharges $\Delta m_f = 6.48$ kg over 1200 s of which only $\Delta m_r = 3.60$ kg is recovered as liquid in the return tank, corresponding to $\eta = 0.554 \pm 0.015$. The pre-cooled configuration (CD1), containing initially $m_{LN_2} = 9.26$ kg of LN_2, discharges $\Delta m_f = 4.62$ kg and recovers $\Delta m_r = 2.99$ kg reaching $\eta = 0.647 \pm 0.018$, a 10 percentage-point improvement attributable to the partially pre-cooled state of the line and return tank.

The measured improvement is consistent with the analysis of Ghaffari-Tabrizi et al. [42], who showed that pre-cooling a cryogenic receiving tank substantially reduces evaporative losses during the fueling transient. In practical settings, however, this gain must be balanced against the cost of the pre-cooling step itself: when liquid nitrogen is used to pre-cool systems operating with other cryogens such as liquid hydrogen, the cumulative nitrogen consumed during chilldown can be large enough that pre-cooling is no longer cost-effective compared with filling the target system directly with its operating fluid [43].

The rewetting of the walls propagates in the direction of the return tank. During experiment CD1 (pre-cooled line), the maxima of $|dT/dt|$ at sensors T2 and T5 are separated by $\Delta t = 10.8$ s, yielding a rewetting-front velocity $u_{rew} = 0.037$ m/s along the 0.40 m transfer section. During experiment CD2 (ambient-temperature line), the two quench fronts are resolved within the DAQ sampling interval so only a lower bound can be reported: $u_{rew} > 0.4$ m/s. As liquid nitrogen enters, it first absorbs heat from the walls, causing boiling and producing a heat peak. Once this boiling phase ends, the liquid flow stops, resulting in a drop and the flow rate returning to zero.

Table 9
Valve states during CD3 experiment phases. 'O' indicates Open and 'C' indicates Closed.

Phase [s]	V1	V2	V3	RV1	RV2	RV3	RV4	RV5
0–10	C	C	C	O	C	C	C	O
10–1125	C	C	C	C	C	O	C	O

The results show that the heat flux absorbed by the nitrogen during the transfer from the feed to the return tank is, as expected, significantly higher in the case of the ambient-temperature line than in the pre-cooled configuration, as also highlighted by Agrawal et al. [44].

Finally, at approximately 1500 s the venting is closed to evaluate the pressure rise in the system, represented in Fig. 8(b).

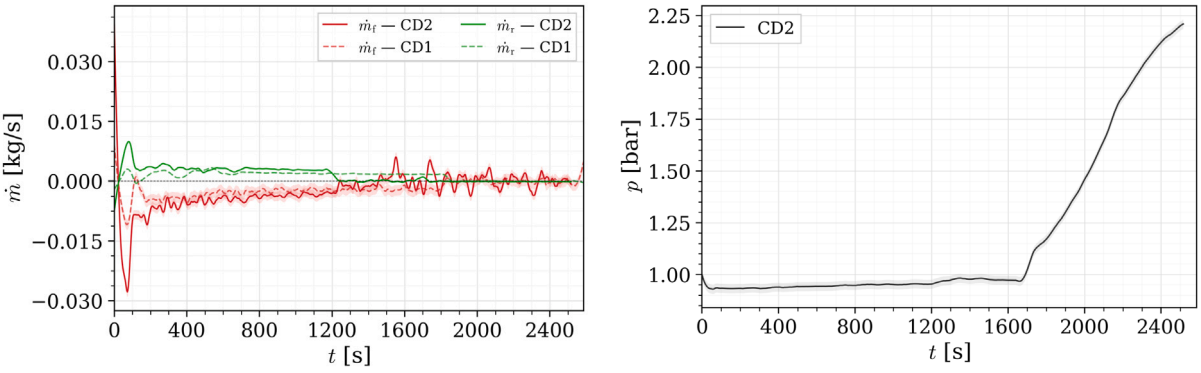
4.3.2. Pressurized transfer

In experiment CD2, a slow chilldown experiment of the return tank was conducted. Before opening the RV3 valve, the feed tank was at ambient pressure, meaning that the liquid level inside the tank was the only driving force for transfer.

In contrast, experiment CD3 involved a fast chilldown of the return tank, with the feed tank initially pressurized to 2 bar. For CD2 and CD3, the feed tank is filled prior to data acquisition, so the initial conditions in Table 4 refer to the state at the start of the transfer phase. Fig. 9(a) shows the temperature trends measured by sensors T1, T2, and T5 for both cases. In the fast chilldown case, the T1 temperature remains almost constant since it is not significantly affected by the liquid transfer process. However, it tends to increase more rapidly because the cryogenic liquid leaves the feed tank faster, giving the tank more time to warm up due to external heat flux.

Temperatures T2 and T5, starting from approximately the same initial values of experiment CD2 ($T_2 = 260.9 \pm 0.7$ K, $T_5 \approx 289.5 \pm 0.8$ K), decrease more quickly during the fast chilldown, but ultimately reach the same steady-state temperature as in the slow chilldown case.

The different filling dynamics are visible in Fig. 9(b). During the unpressurized transfer (CD2) the return tank level increases smoothly to 49.77 ± 0.11 cm over the 1200 s of the transfer period, while the feed-tank level decreases to about 16.00 ± 0.17 cm. In contrast, during the pressurized transfer (CD3), the elevated driving pressure discharges the feed tank inventory in less than 100 s, before the transfer line



(a) Mass flow rate inside the feed and return tanks

(b) Absolute pressure rise due to closure of venting at approximately 1500s during experiment CD2

Fig. 8. On the left, (a), comparison of mass flow rates during transfer with non pre-cooled (CD2) and pre-cooled (CD1) return tank. On the right, (b), absolute pressure for run CD2.

and return tank could undergo substantial progressive cooling: delivery ceases not by valve action but by feed exhaustion, approximately at the instant H_r peaks. As a result, the return-tank level signal does not exhibit a corresponding monotonic rise: a transient excursion of H_r is recorded during the discharge, peaking near 25.65 ± 0.11 cm at $t \approx 74$ s and subsequently decaying to an asymptotic value of 10.80 ± 0.10 cm after about 500 s from valve opening. This behavior indicates that the return tank response is regulated by the competition between the duration of liquid transfer and the thermal response of the initially warm receiving hardware. To quantify this effect an experimental transfer-to-cooling time ratio is defined as

$$\Pi_t = \frac{t_{\mathrm{tr}}}{t_{\mathrm{cool}}} \tag{9}$$

where t_{tr} is the duration of active liquid transfer and t_{cool} is the time required for the return-side wall temperature T_5 to reach a prescribed cooling criterion. Here, t_{transfer} is measured from the opening of valve RV3 to the end of sustained feed-tank outflow and for t_{cool}, a common threshold of $T_5 = 150$ K is applied to both runs, such that

$$t_{\mathrm{cool}} = t(T_5 = 150\ \mathrm{K}) - t_{\mathrm{RV3,open}} \tag{10}$$

This definition is based directly on the measured wall-temperature response and is independent of the amount of liquid ultimately recovered in the return tank. The ratio Π_t therefore provides an experimental measure of whether liquid transfer persists long enough for substantial progressive cooling of the receiving-side wall for the present experimental configuration. Values $\Pi_t < 1$ indicate that transfer is completed before the wall reaches the prescribed cooling state, whereas $\Pi_t > 1$ indicates that transfer persists for longer than the corresponding cooling time.

For CD2, the active transfer duration is approximately 1180 s, while the $T_5 = 150$ K cooling criterion is reached after approximately 263 s, giving $\Pi_t \approx 4.49$. In CD3, the corresponding values are approximately 113 s and 240 s, respectively, giving $\Pi_t \approx 0.47$. Thus, the unpressurized transfer persists for several wall-cooling times, whereas the pressurized transfer terminates before the receiving-side wall reaches the same cooling state. Importantly, the measured cooling times themselves are similar in the two runs, differing by only approximately 9%, while the transfer durations differ by more than an order of magnitude. The resulting separation in Π_t is therefore primarily caused by the substantially shorter transfer duration in CD3 rather than by a fundamentally different thermal response of the return-side wall. The conclusion is not sensitive to the particular temperature threshold selected. For cooling criteria between 175 and 100 K, Π_t remains greater than unity for CD2 and below unity for CD3, with values ranging from approximately 5.72 to 1.36 for CD2 and from 0.75 to 0.12 for CD3. This robustness indicates that the observed separation reflects the substantially different transfer durations rather than an arbitrary choice of cooling criterion.

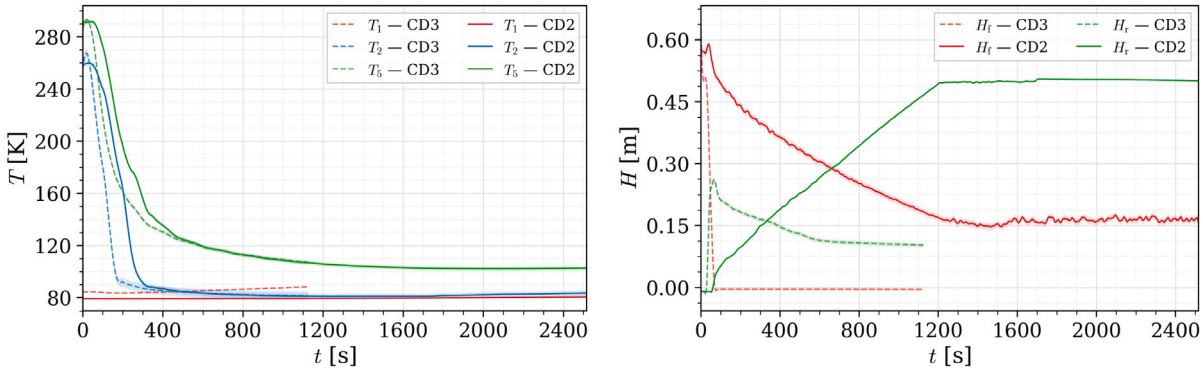
The difference in timescales has a direct impact on transfer efficiency. CD3 discharges $\Delta m_f = 8.42$ kg from the feed tank in less than 100 s but recovers only $\Delta m_r = 0.88$ kg as liquid in the return tank ($H_r \approx 10$ cm), resulting in $\eta = 0.104 \pm 0.003$ compared with $\eta = 0.554 \pm 0.015$ in CD2 for the same fluid inventory and essentially identical initial wall temperature. Although the total wall enthalpy that must be removed is the same in both runs, the slower transfer of CD2 allows progressive cooling of the walls, so that the liquid arriving later encounters a partially chilled system and undergoes less evaporation. The main difference is therefore the time available for this heat removal to occur while liquid is being supplied. In CD3, the full inventory is transferred before substantial wall cooling can occur, so a larger fraction of the liquid is exposed to the initial wall superheat and vaporized. The generated vapor is continuously discharged through valve RV5 without any liquid actually accumulating in the return tank.

Although increasing the driving pressure shortens the transit time, it does not reduce the initial wall heat load; instead, it concentrates the heat exchange into a shorter interval, thereby increasing the fraction of liquid vaporized during transfer.

The mass flow rate profiles in Fig. 10 reflect the order-of-magnitude difference in active transfer duration between the two configurations. During CD3, the feed-tank outflow peaks at approximately 0.183 ± 0.003 kg/s and decays to zero within about 130 s, whereas in CD2 the flow rates are substantially lower but sustained over approximately 1260 s. In both cases the return-tank inflow is consistently smaller than the feed-tank outflow, confirming that a significant fraction of the liquid evaporates within the warm transfer line and return tank. This vapor generation is amplified at higher driving pressure, which forces larger liquid inventory into the warm line per unit time [44,45]. The integrated transfer efficiencies reported in Table 4 and described above, quantify the cumulative effect: the slower unpressurized transfer permits progressive cooling of the line and return-tank walls, reducing the evaporative penalty for liquid arriving later in the process; the pressurized transfer, by contrast, exposes the full inventory to the initial wall superheat before any significant pre-cooling can occur. This inherent compromise between transfer speed and cryogenic losses is consistent with the time–mass trade-off identified in numerical studies of cryogenic loading [46] and are interpreted through a common theoretical framework in Section 5.1.

4.4. Boil-off tests

Boil-off tests were conducted under two conditions: ambient heat leak alone and controlled electrical heating via the immersed heater in the feed tank (EH1 in Fig. 1(b)). In both cases, all vent valves were kept



(a) Wall feed tank temperature (T1) and inlet/outlet transfer section temperatures (T2 and T5) history

(b) Feed (H_f) and return (H_r) liquid level history during chilldown

Fig. 9. Temperature and liquid level trends comparison during transfer with pressurized (CD3) and ambient pressure (CD2) feed tank.

Table 10
Valve states during boil-off experiments (BO1–BO3, FBO1, FBO2). 'O' indicates Open and 'C' indicates Closed.

Phase	V1	V2	V3	RV1 - RV5	EH1
All phases	C	C	C	C	Off/ On[a]

[a] EH1: immersed electrical heater. Off for BO1-BO3; On at the specified power level (Table 11) for FBO1, FBO2.

Table 11
Summary of boil-off runs. $T_{1,0}$: initial feed-tank wall temperature (sensor T1); p_0: initial feed tank absolute pressure (mechanical pressure gauge PI1); $m_{LN_2,0}$: initial LN_2 mass in feed tank; P_{heater}: input to power supply; $T_{1,f}$: final feed-tank wall temperature (sensor T1); Δp: feed tank pressure rise (mechanical pressure gauge PI1).

Run	Initial conditions				Outcome metrics		
	$T_{1,0}$ [K]	p_0 [bar]	$m_{LN_2,0}$ [kg]	P_{heater} [W]	$T_{1,f}$ [K]	Δp [bar]	Duration [s]
BO1	79.2	1	3.0	–[a]	86.4	1.2	7095
BO2	79.3	1	3.8	–[a]	85.4	1.1	6060
BO3	79.1	1	8.2	–[a]	83.4	1	6110
FBO1	78	1	2.9	20 → 45 → 55[b]	90.7	1.5	4600
FBO2	79.2	1	8.2	45	84.2	1	1860

[a] Heater off.

[b] FBO1 employs a stepped heater-power profile ($P_1 \rightarrow P_2 \rightarrow P_3$). The 55 W step was applied for 600 s; the segment did not reach a quasi-steady plateau and is therefore not analyzed quantitatively.

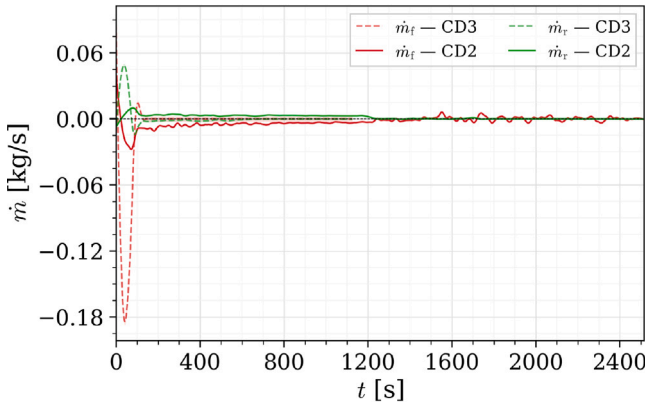


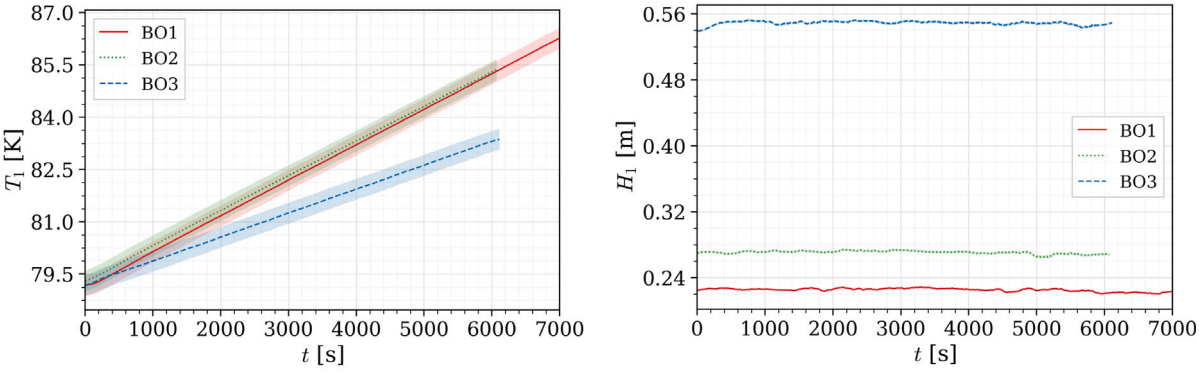
Fig. 10. Mass flow rate inside the feed and return tanks during transfer with pressurized (CD3) and ambient pressure (CD2) feed tank.

closed throughout the run. Three fill levels were investigated under natural boil-off conditions (runs BO1 to BO3), and two forced boil-off runs (FBO1 and FBO2) were conducted at low and high fill levels, respectively. The experimental conditions for each run are summarized in Table 11.

4.4.1. Natural convection

Fig. 11(a) shows the wall feed tank temperature (T1) versus time for three runs with different initial LN_2 masses. All three traces are approximately linear in time, confirming that the feed tank operates in a quasi-steady self-pressurization regime dominated by ambient heat in-leak. However, the red line (BO1, $m_{LN_2} = 3.0$ kg) exhibits a slightly steeper slope ($dT_1/dt = 1.020 \pm 0.003$ mK/s) compared to the green dashed line (BO2, $m_{LN_2} = 3.8$ kg) slope ($dT_1/dt = 0.998 \pm 0.003$ mK/s), indicating a faster temperature rise, consistent with the lower liquid inventory shown in Fig. 11(b). On the other hand, the blue dashed line (BO3, $m_{LN_2} = 8.2$ kg) exhibits a more moderate slope ($dT_1/dt = 0.687 \pm 0.002$ mK/s) due to the bigger mass of LN_2, which is almost double that of the other two cases. The observed reduction in dT_1/dt as the initial inventory increases is consistent with the influence of liquid thermal inertia.

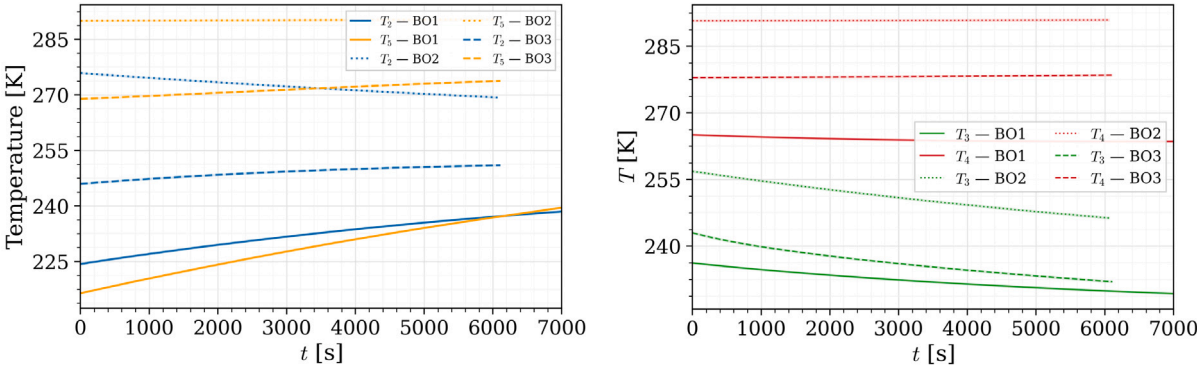
Figs 12(a) and 12b present the transfer section and thermal shield temperatures, respectively. Since no flow goes through the test section or in the thermal shield, the temperatures remain relatively stable throughout the observation period. The convergence of T2 toward 240 K for all three runs, despite different initial values spanning 220–275 K, reflects axial conduction from the feed-tank flange, which acts as a thermal bridge between the cold liquid and the ambient-temperature transfer section. Thermal shield temperatures (T3, T4) are stable to within ±5 K over each run, confirming that the 30-layer MLI



(a) Comparison of wall feed tank temperature (T1)

(b) Comparison of liquid levels in the feed tank

Fig. 11. Temperature T1 and liquid level trends for the boil-off of three different fill levels in the feed tank with heater off.



(a) Comparison of inlet (T2) and outlet (T5) temperatures of test section

(b) Comparison of thermal shield temperatures T3 and T4

Fig. 12. Temperatures T2 to T5 for the boil-off of three different LN_2 masses in the feed tank with heater off.

shield is intercepting the bulk of the ambient radiation load and that the inner-vessel boil-off is not significantly perturbed by shield transients. Finally, Fig. 13 shows the wall stored energy rate q_w^* decreasing from approximately 6.5 ± 0.4 W/m^2 (BO1, 25% fill) to 4 ± 0.3 W/m^2 (BO3, 68% fill), reflecting the lower self-pressurization rate at higher liquid inventory.

Overall, these preliminary experiments demonstrate that higher liquid filling levels lead to larger thermal inertia and a correspondingly reduced temperature rise. When the liquid level decreases, the wetted wall area shrinks and a larger portion of the tank wall becomes exposed to vapor, which is less effective at removing heat; consequently, the gas temperature and tank pressure increase more markedly, enhancing vaporization and intensifying the boil-off phenomenon. The natural boil-off results establish a baseline: the effective heat leak to the inventory scales with wetted wall area. Any additional heat load, such as that imposed by the immersed electrical heater in the forced boil-off runs, should therefore manifest as an additive contribution.

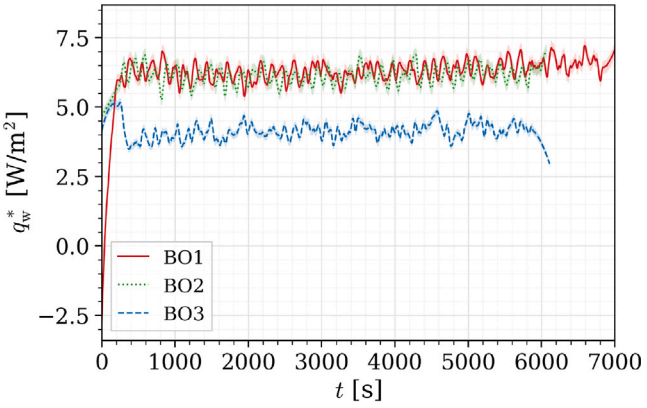
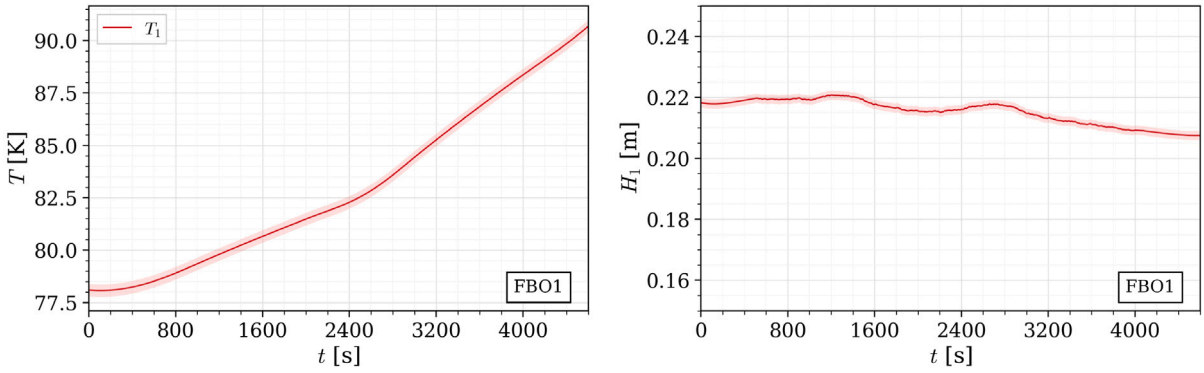


Fig. 13. Wall stored energy rate during the three boil-off experiments with heater off.

4.4.2. Forced convection

Run FBO1 and FBO2 represent the first use of the facility's immersed electrical heater, a feature included in the initial design by De Salve and Panella [35] but not employed in any previously reported experimental campaign. The objective of these tests is twofold: to establish that the heater can deliver a reproducible and controllable thermal load to the inventory (FBO1, two heat-input steps at low fill), and to quantify the incremental heat flux it imposes relative to natural boil-off (FBO2 versus BO3, at matched fill level). The immersed electrical heater described in Section 2 is connected to an external power supply through the heater port on the top flange of the feed tank. FBO1 was conducted at a reduced fill level of $H_{f,0} = 21.9 \pm 0.1$ cm ($\approx$ 35% of capacity) to maximize the sensitivity of T1 to the imposed heat input. A staircase power profile was applied: 20 W from $t = 0$ s to $t \approx 2500$ s then increased to 45 W until $t \approx 4000$ s, with a brief 55 W pulse of 600 s at the end to probe the system response at higher power. The 55 W segment is too short to reach a quasi-steady plateau and is shown in Fig. 14 for completeness but is not analyzed quantitatively. The analysis below is restricted to the 20 W and 45 W plateaus.

Fig. 14(a) shows the temperature evolution at sensor T1. Three slope regions are clearly visible, corresponding to the three power levels. Values reported are $dT_1/dt = 1.894 \pm 0.020$ mK/s at 20 W and $dT_1/dt = 3.881 \pm 0.019$ mK/s at 45 W. The ratio $3.88/1.89 \approx 2.05$ is close to the



(a) Wall feed tank temperature (T1) increase with heater on and no venting

(b) Liquid level with heater on and no venting

Fig. 14. Temperature T1 and liquid level for the boil-off experiment with heater on during experiment FBO1.

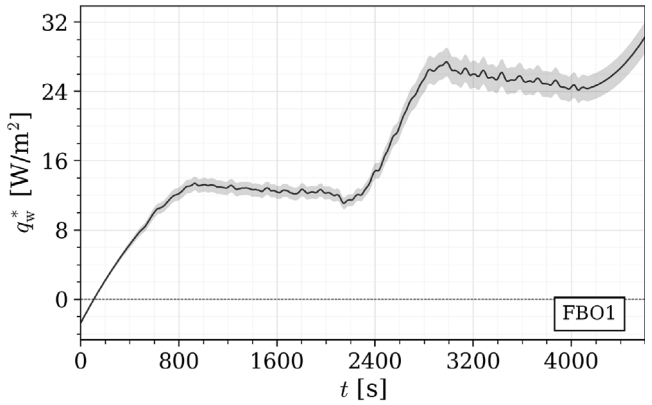


Fig. 15. Wall stored energy rate during experiment FBO1.

Table 12
Quasi-steady boil-off slopes, obtained by OLS linear regression on T_1 over the quasi-steady window of each run. Uncertainties are expanded ($K = 2$) and the coefficient of determination of the fit $R^2_{T_1}$ is also reported.

Run	dT_1/dt [mK/s]	$R^2_{T_1}$
BO1	1.020 ± 0.003	0.999975
BO2	0.998 ± 0.003	0.999969
BO3	0.687 ± 0.002	0.999984
FBO1 @ 20 W	1.894 ± 0.020	0.996593
FBO1 @ 45 W	3.881 ± 0.019	0.999707
FBO2	2.846 ± 0.010	0.999980

power ratio $45/20 = 2.25$, indicating a near-linear wall thermal response in this range.

The initial transient ($\approx$ 200 s) visible in Fig. 15 corresponds to the thermal relaxation of the wall following tank closure and heater activation, during which the wall briefly loses stored energy to the liquid.

To isolate the contribution of the immersed heater to the total evaporative heat load, FBO2 was conducted at a higher fill level of $H_{f,0} = 51.3 \pm 0.1$ cm with a constant 45 W heater power. This experiment is compared against the first 2000 s of natural boil-off run BO3, which was conducted at a comparable initial fill level ($H_{f,0} = 54.1 \pm 0.2$ cm) and described in Section 4.4.1. The direct comparison of FBO2 and BO3 in Fig. 16 and Fig. 17 highlights the heater contribution. Over the $0 \leq t \leq 1800$ s window, FBO2 shows a T1 slope of 2.85 ± 0.01 mK/s versus 0.687 ± 0.002 mK/s for BO3, a factor of 4 increase attributable entirely to the heater. Fig. 17 shows that in FBO2 the heater elevates the wall stored energy rate q^*_w by approximately 12 W/m^2 relative to BO3. This wall storage increment represents only one of the contributions to the total heat load imposed by the heater: the full partition between wall storage, liquid sensible heating, and net phase change is analyzed in Section 5.2. A differential energy balance derived in Appendix A.1 is then used to close the energy budget against the nominal heater input, providing an independent validation of the measurement chain.

5. Discussion of results

Section 4 presented the measured cooling curves, transfer efficiencies, and self-pressurization rates in dimensional form. The following discussion expands on these findings and examines the underlying trends and their relevance beyond the individual test conditions. The efficiencies of the three chilldown runs are compared in Section 5.1 with a theoretical value and the tests are presented in a non-dimensional form to analyze how the choice of driving pressure and pre-cooling influences the trade-off between chilldown time and propellant consumption. Section 5.2 analyzes the closed tank boil-off measurements from an energy-partitioning perspective and discusses their implications for hold-time estimation.

5.1. Chilldown strategy

The three runs CD1-tr, CD2 and CD3, cover different combinations of initial wall temperature and driving pressure while using the same receiving hardware. The difference in measured efficiency therefore reflects both the thermal demand of the chilldown and the effectiveness of the transfer process. To separate these effects, the liquid expelled from the feed tank is considered in terms of three contributions: the liquid delivered to the return tank, the liquid theoretically required to cool the receiving hardware and the remaining non-delivered fraction.

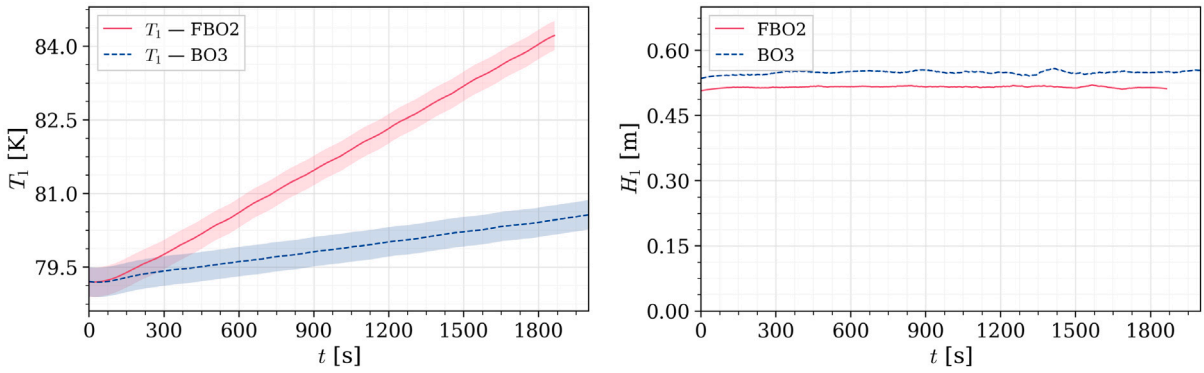
The total energy required to cool the receiving hardware from its pre-transfer state to the final wall temperature is

$$Q_{\mathrm{cd}} = \sum_{i\in\{\mathrm{line,ret}\}} m_{w,i} \int_{T_{f,i}}^{T_{0,i}} c_{p,\mathrm{SS}}(T)\,\mathrm{d}T \tag{11}$$

where $m_{w,\mathrm{line}}$ and $m_{w,\mathrm{ret}}$ are the wall masses of the transfer line and return tank, respectively. The temperature-dependent specific heat, $c_{p,\mathrm{SS}}(T)$, is taken from the NIST cryogenic materials database [38].

The corresponding amount of liquid mass required to provide this energy is

$$m_{\mathrm{req}} = \frac{Q_{cd}}{h_{fg}} \tag{12}$$



(a) Wall feed tank temperature (T1) increase with heater on and no venting

(b) Liquid level with heater on and no venting

Fig. 16. Temperature T1 and liquid level comparison for forced boil-off experiment FBO2 and natural boil-off experiment BO3.

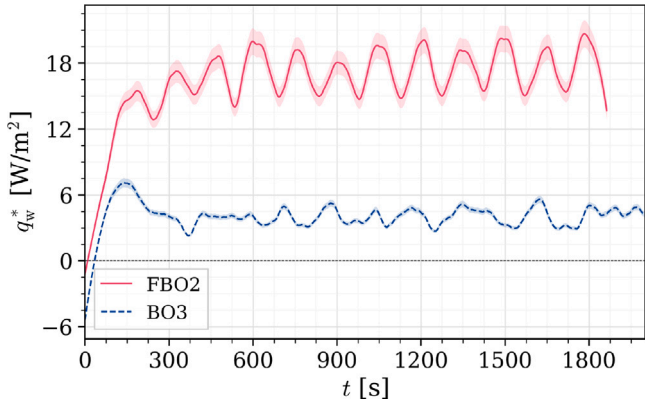


Fig. 17. Wall stored energy rate comparison for forced boil-off experiment FBO2 and natural boil-off experiment BO3.

where h_{fg} is the latent heat of vaporization of the liquid. Referring this value to the mass expelled from the feed tank gives the chilldown mass fraction:

$$\eta_{\mathrm{cd}} = \frac{m_{\mathrm{req}}}{\Delta m_f} = \frac{Q_{\mathrm{cd}}}{\Delta m_f\, h_{fg}} \tag{13}$$

which represents the liquid mass fraction of the expelled liquid required to produce the calculated chilldown energy. The quantity η_{cd} introduced here is related to the thermal efficiency parameter of Hartwig et al. [47], in which the amount of fluid consumed during chilldown is used to characterize thermal utilization. Here, it is used specifically to identify the thermodynamic-minimum component of the Δm_f mass budget. This minimum requirement defines a theoretical upper bound against which the measured transfer efficiency η can be compared. If η denotes the measured transfer efficiency defined using Eq. (2) in Section 3, then, under the idealized assumption that the minimum chilldown requirement is the only unavoidable consumption of the expelled liquid, the maximum achievable delivery fraction is

$$\eta_{\mathrm{max,theo}} = 1 - \eta_{\mathrm{cd}} \tag{14}$$

The remaining fraction of the expelled liquid that is not accounted for by the measured delivery or the minimum chilldown requirement is defined as

$$\eta_{\mathrm{res}} = 1 - \eta - \eta_{\mathrm{cd}} \tag{15}$$

and represents the combined effect of different loss mechanisms, comprising ambient heat leak, venting, and imperfect wall–fluid coupling.

Finally, it is possible to define a transfer effectiveness relative to the theoretical upper bound as

$$\varepsilon_{\mathrm{tr}} = \frac{\eta}{\eta_{\mathrm{max,theo}}} \tag{16}$$

Table 13 collects the measured transfer efficiency, minimum chilldown fraction, theoretical upper bound, transfer effectiveness, and residual fraction for the three runs. Fig. 18 summarizes the wall-enthalpy demand and the corresponding mass-budget quantities.

The measured efficiency η is below the theoretical value $\eta_{\mathrm{max,theo}}$ in all three runs, as expected since the benchmark accounts only for the minimum energy required for chilldown. The corresponding transfer effectiveness $\varepsilon_{\mathrm{tr}} = \eta/\eta_{\mathrm{max,theo}}$ provides a direct check of how closely the measured transfer approaches this thermodynamic limit. In terms of procedure effectiveness, CD1-tr and CD2 give similar values, $\varepsilon_{\mathrm{tr}} = 0.74$ and 0.76, respectively, while their measured efficiencies differ more noticeably, at 0.65 and 0.55, respectively. The difference is primarily associated to the lower wall energy demand for CD1-tr, where pre-cooling the system reduces Q_{cd} from 330 to approximately 108 kJ. Consequently, η_{cd} goes from 0.27 for CD2 to 0.12 for CD1-tr. This behavior is consistent with the observation of Ghaffari-Tabrizi et al. [42] that pre-cooling improves the delivered fraction while leaving the underlying evaporative mechanism unchanged.

CD3 shows a different behavior: its chilldown energy demand is essentially identical to that of CD2 with Q_{cd} = 327 kJ compared with 330 kJ for CD2. The resulting η_{cd} is also comparable, with 0.22 for CD3 and 0.27 for CD2. However, the measured efficiency regarding the delivered liquid fraction falls to 0.10. As a consequence, CD3 procedure effectiveness is substantially lower (0.13 versus 0.75 for CD2). This suggests that the difference between CD2 and CD3 is unlikely to be explained by the thermal mass demand alone and instead points to additional losses or inefficiencies during the delivery process. As in CD3 the full inventory is exposed to the initial wall superheat before significant progressive cooling can occur, which is consistent with the large residual fraction, $\eta_{\mathrm{res}} = 0.68$.

To provide a common comparison of the thermal state, the temperature can be non-dimensionalized as

$$\Theta = \frac{(T - T_{\mathrm{sat}})}{(T_{\mathrm{amb}} - T_{\mathrm{sat}})} \tag{17}$$

where T_{sat} = 77.36 K and T_{amb} = 293.15 K. A normalized time is defined as

$$\hat{t} = \frac{t}{t_{\mathrm{ref}}} \tag{18}$$

where t_{ref} = 1400s denotes the cooling duration of the return tank side in CD2. Thus, $\hat{t} = 1$ corresponds to completion of the chilldown transient under the CD2 reference condition and provides a common time scale for comparing the three tests. To provide a common comparison of

Table 13
Mass-budget partition of the LN_2 expelled from the feed tank during each transfer run. η: measured efficiency; η_{cd}: minimum chilldown mass fraction; $\eta_{max,theo}$: theoretical upper bound; η_{res}: residual non-delivered fraction; ε: transfer effectiveness.

Run	η [–]	η_{cd} [–]	$\eta_{max,theo}$ [–]	η_{res} [–]	ε_{tr} [–]
CD1-tr	0.647 ± 0.018	0.123 ± 0.009	0.877 ± 0.009	0.230 ± 0.021	0.737 ± 0.023
CD2	0.554 ± 0.015	0.271 ± 0.020	0.729 ± 0.020	0.175 ± 0.027	0.759 ± 0.032
CD3	0.104 ± 0.003	0.216 ± 0.016	0.784 ± 0.016	0.680 ± 0.017	0.132 ± 0.005

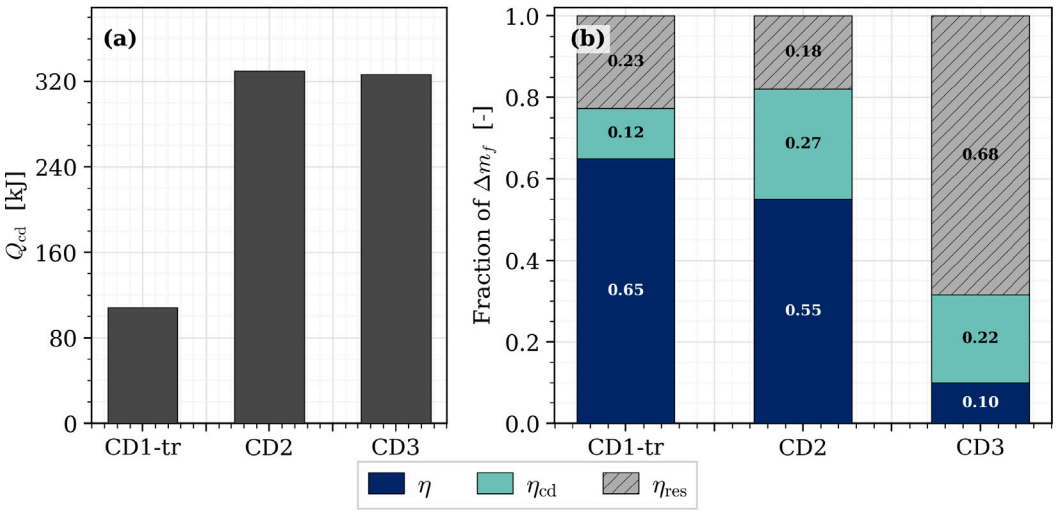


Fig. 18. (a) Wall enthalpy demand Q_{cd} from Eq. (11) (b) Mass-budget partition of the LN_2 expelled from the feed tank into: the delivered fraction $\eta = \Delta m_r/\Delta m_f$, the thermodynamic minimum required to chill the receiving hardware $\eta_{cd} = m_{req}/\Delta m_f$, and the residual non-delivered fraction η_{res}. The three fractions sum to unity by construction.

liquid consumption, the normalized feed mass consumption is defined as

$$\hat{m} = \frac{m_f}{m_{ideal}} \tag{19}$$

where m_f is the mass being drawn from the feed tank and m_{ideal} is the theoretical liquid-nitrogen mass required to supply the sensible energy needed to cool the receiving hardware from the common ambient reference temperature to saturation, assuming that the entire latent heat of the liquid is available for wall cooling. Here, m_{ideal} is evaluated from Eqs. (11) and (12) using T_{amb} and T_{sat} as the limiting temperatures rather than the initial and final temperatures of each experiments. Consequently, $\hat{m}$ should be interpreted as a normalized received liquid mass rather than a run-specific requirement.

Fig. 19 presents the resulting non-dimensional comparison. In panel (a), the evolution of Θ_5 with $\hat{t}$ shows the time required for the receiving hardware to reach a given thermal state relative to the CD2 cooling duration. In panel (b), the corresponding evolution with $\hat{m}$ shows the feed-side liquid consumption associated with that thermal state. Thus, for a given value of Θ_5, the two representations provide complementary measures of chilldown performance: a smaller $\hat{t}$ indicates faster cooling, while a smaller $\hat{m}$ indicates that the same thermal state is reached with less liquid consumption. The comparison also highlights the effect of the initial thermal condition, since CD1-tr begins with a partially pre-cooled receiving system, whereas CD2 and CD3 begin from approximately ambient conditions. In CD3, liquid transfer terminates before the receiving wall reaches its cooled state with $\Theta_5 \approx 0.77$. The subsequent vertical segment $\Theta_5 - \hat{m}_f$ trajectory reflects continued thermal evolution after feed-tank exhaustion.

Taken together, the results show that chilldown performance cannot be represented by a single efficiency or time metric. For a given thermal state, the $\hat{t}$ and $\hat{m}$ representations provide complementary measures of performance: the former quantifies the time required to reach the state, while the latter quantifies the associated liquid consumption. Pre-cooling shifts this balance favorably by reducing the initial wall enthalpy that must be removed, while increasing the driving pressure, in contrast, substantially accelerates liquid transfer but does not reduce the underlying thermal demand of the initially warm receiving hardware. The 2 bar case therefore reaches the transfer endpoint much faster, but with a delivered fraction of only 10% and a residual non-delivered fraction of 68%.

From an operational perspective, these results indicate that no single chilldown strategy is optimal for all objectives. When cryogen utilization or liquid retention is the primary constraint, pre-cooling is advantageous because it reduces the thermal demand and the associated minimum chilldown mass. When rapid thermal conditioning is the dominant requirement, pressure-driven transfer can provide a substantial reduction in transfer time, but the resulting loss of liquid retention must be accounted for. More generally, the appropriate strategy depends on the relative importance assigned to conditioning time, cryogen expenditure and the amount of liquid that must ultimately be retained in the receiving system. The present measurements therefore provide experimentally grounded guidance for selecting the operating strategy according to the relevant system constraint, rather than identifying a single universally optimal condition.

Eqs. (11)–(15) can be applied to other cryogenic fluids by using the corresponding thermophysical properties, while the wall-mass inventory remains a system-specific input. This allows the thermodynamic minimum required for chilldown, the corresponding theoretical upper bound, and the residual loss fraction to be evaluated within the same framework for different cryogens. Table 14 compares the saturated-fluid properties for LN_2, LOX, LCH_4 and LH_2 at 1 atm, together with the per-fluid value of the dimensionless maximum specific liquid requirement

$$\sigma_{max} \equiv \frac{\bar{c}_w \, \Delta T_m}{h_{fg}}, \tag{20}$$

originally introduced by Jacobs [48] and revisited by Zong [49], where $\bar{c}_w$ is the receiving-wall specific heat averaged over $\Delta T_m = T_{amb} -$

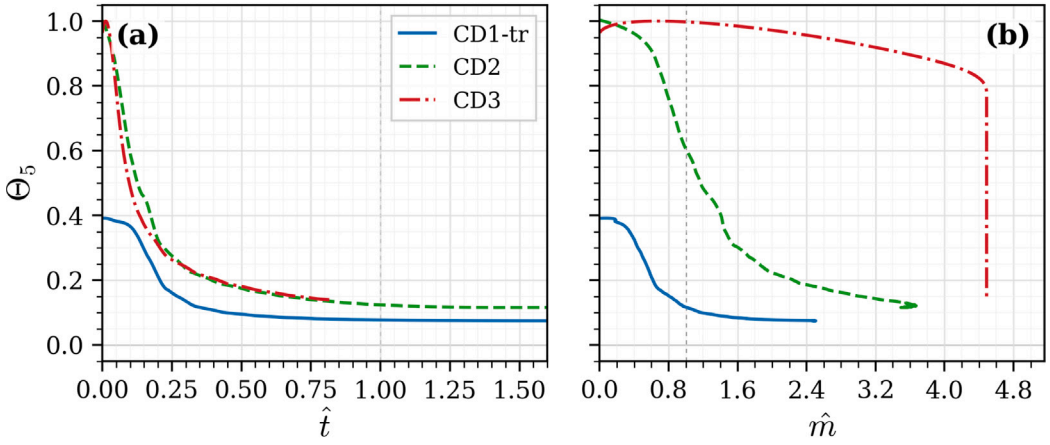


Fig. 19. Non-dimensional comparison of receiving-side thermal state during chilldown. (a) Normalized return-side wall temperature Θ_5 versus normalized time $\hat{t}$ (b) Θ_5 versus normalized delivered mass $\hat{m}$, referenced to the theoretical latent-only mass required to cool the receiving hardware from the common ambient reference state.

T_{sat} [38], and h_{fg} is the coolant latent heat at saturation. Physically, σ_{max} is the maximum coolant mass required, per unit mass of receiving-wall material, to carry the wall from ambient to the saturation state, under the latent-only limit in which the vapor leaves at T_{sat} without sensible-heat utilization. Thus, it should be regarded as an upper bound, since in practice some of the vapor's sensible enthalpy is also transferred to the wall, meaning that less liquid is needed than this estimate suggests [48,49]. This effect is most pronounced for LH_2, which has a high vapor heat capacity. The LH_2 scaling presented below should therefore be interpreted as a conservative estimate. Substituting Eq. (20) in the chilldown mass balance underlying Eq. (13) shows that σ_{max} enters η_{cd} directly, so that, at fixed hardware mass ratio $m_w/\Delta m_f$, η_{cd} scales linearly across fluids with σ_{max} alone. Taking the present LN_2 configuration as reference, Table 14 shows that σ_{max} takes the values 0.90, 0.35 and 0.48 relative to LN_2 for LOX, LCH_4 and LH_2 respectively. Under identical hardware mass ratio, the chilldown mass fraction η_{cd} is therefore predicted to be 10% smaller than the LN_2 value for LOX, and smaller by factors of approximately 2.9 and 2.1 for LCH_4 and LH_2. Through Eq. (14), this scaling propagates directly to the theoretical efficiency, $\eta_{max,theo} = 1 - \eta_{cd}$. These differences provide a quantitative indication of the extent to which the thermophysical conditions underlying the present LN_2 analysis vary across cryogens, while the same methodology can be retained by substituting the appropriate fluid properties.

5.2. Boil-off energy partition and implication for hold-time

Section 4.4.2 characterized the boil-off runs in term of the wall stored energy rate q_w^*, showing that the heater increases this value by approximately 12 W/m^2 relative to a natural boil-off run with the same liquid inventory. However, the heat load imposed by the heater can be divided into different contributions. Liquid sensible heating is expected to dominate, as the liquid heat capacity is roughly an order of magnitude greater than that of the wall. Moreover, self-pressurization raises the saturation temperature, requiring the liquid to absorb sensible energy before further net evaporation can occur. To quantify the relative importance of the different terms, the closed tank first law in Eq. (28) is evaluated for each run. Expanding $du_m/dT|_{sat}$ according to Eq. (29) yields four contributions, all proportional to dT_1/dt. These are the sensible heating of the liquid,

$$\dot{Q}_{liq} = m\,(1-x)\,\left.\frac{du_l}{dT}\right|_{sat}\frac{dT_1}{dt} \tag{21}$$

the sensible heating of the vapor,

$$\dot{Q}_{vap} = m\,x\,\left.\frac{du_v}{dT}\right|_{sat}\frac{dT_1}{dt} \tag{22}$$

Table 14
Saturated-fluid properties at p = 1 atm for the cryogens considered. The value σ_{max} is defined as in Eq. (20), $\bar{c}_w$ is the SS304 specific heat averaged over $\Delta T_m = T_{amb} - T_{sat}$, with T_{amb} = 300 K. Ratios in the last block are referred to LN_2.

Property	LN_2	LOX	LCH_4	LH_2
T_{sat} [K]	77.35	90.19	111.67	20.27
h_{fg} [kJ/kg]	199.2	213.1	510.8	446.1
ρ_l [kg/m^3]	806.1	1141.2	422.4	70.8
ρ_v [kg/m^3]	4.612	4.467	1.816	1.339
ρ_l/ρ_v [–]	175	255	233	53
$c_{p,l}$ [J/(kg K)]	2041	1699	3481	9729
$c_{p,v}$ [J/(kg K)]	1124	971	2218	12 028
k_l [W/(m K)]	0.145	0.151	0.184	0.101
μ_l [μPa s]	160.7	194.7	116.9	13.5
$\Delta T_m = T_{amb} - T_{sat}$ [K]	222.6	209.8	188.3	279.7
$\bar{c}_w$ (SS304) [J/(kg K)]	389	398	412	329
σ_{max} [–]	0.434	0.392	0.152	0.206
$h_{fg}/h_{fg,LN_2}$	1.00	1.07	2.56	2.24
$\Delta T_m/\Delta T_{m,LN_2}$	1.00	0.94	0.85	1.26
$\sigma_{max}/\sigma_{max,LN_2}$	1.00	0.90	0.35	0.48

the net phase-change contribution,

$$\dot{Q}_{lat} = m\,(u_v - u_l)\,\frac{dx}{dT}\,\frac{dT_1}{dt} \tag{23}$$

and the wall storage term,

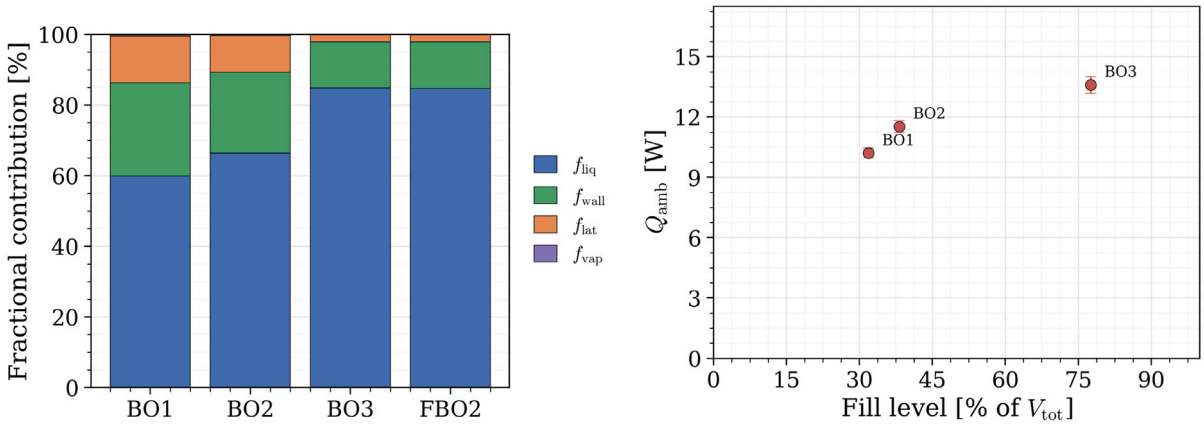
$$\dot{Q}_{wall} = m_w\,c_w(T_1)\,\frac{dT_1}{dt} \tag{24}$$

The inventory m is fixed at its initial value (Table 11) while the volume constraint $v_m = V_{tank}/m$ determines the quality $x(T_1)$ through Eq. (27). The ambient heat in-leak $\dot{Q}_{amb}$ can be calculated as the residual of Eq. (28):

$$\dot{Q}_{amb} = \dot{Q}_{liq} + \dot{Q}_{vap} + \dot{Q}_{lat} + \dot{Q}_{wall} - P_{heater} \tag{25}$$

Table 15 reports the four contributions and $\dot{Q}_{amb}$ with $K = 2$ expanded uncertainties for the runs BO1, BO2, BO3 and FBO2; FBO1 is omitted for the reasons discussed in Section 4.4.2. Under the quasi-steady closed tank conditions considered here, the wall term can also be written as $\dot{Q}_{wall} = q_w^*\,A_{inner}$, where A_{inner} is the total inner surface of the feed-tank shell. The resulting wall contribution agrees with the q_w^* values shown in Fig. 13 to within 0.02 W for all runs.

Fig. 20(a) shows the relative contribution of each term to the total energy budget $P_{heater} + \dot{Q}_{amb}$. Across the natural boil-off runs, the liquid sensible contribution increases from 60% of at low fill (BO1) to 85% at the highest fill level (BO3). Over the same range, wall storage



(a) Fractional contributions to the closed tank energy budget, $P_{heater} + \dot{Q}amb$, from liquid sensible heating (Q_{liq}), wall storage (f_{wall}), net phase change (f_{lat}), and vapor sensible heating (f_{vap}) for each run. FBO1 is excluded as discussed in Section 4.4.2.

(b) Ambient heat in-leak $\dot{Q}_{amb}$ as a function of feed-tank fill level (percentage of V_{tot}), obtained as the residual of Eq. (28) for BO1–BO3. Error bars denote $K = 2$ expanded uncertainties, reported in Table 15.

Fig. 20. Closed tank energy balance and ambient heat in-leak. (a) Energy budget partition and (b)Ambient heat leak as a function of fill level.

decreases from 26% to 13% while the net phase change contribution decreases from 13% to 2%. The vapor sensible contribution is below 0.1% in every run. Fig. 20(b) shows the ambient heat leak as a function of the fill level. For the natural boil-off runs, $\dot{Q}$amb increases from 10.21 ± 0.25 W at 25% fill (BO1) to 13.59 ± 0.42 W at 68% fill (BO3). At matched inventory ($m = 8.2$ kg), FBO2 recovers $\dot{Q}_{amb} = 11.47 \pm 1.96$ W, about 2.2 W below the BO3 value: this offset corresponds to the fraction of heater power not recovered in the differential closure for which $\Gamma = 0.95 \pm 0.02$ (Eq. (31), Appendix A.1).

The energy partition has a direct implication for the interpretation of boil-off under closed-tank conditions. Across the natural boil-off experiments, the fraction of the incoming heat absorbed as liquid sensible energy increases from 60% to 85% as the fill level increases, while the net phase-change contribution decreases from 13% to 2%. Thus, only a small fraction of the ambient heat leak contributes to the change in vapor–liquid partition over the investigated range, with the dominant contribution instead absorbed through sensible heating of the inventory and storage in the tank wall. This distinction is important when relating ambient heat leak to boil-off losses or hold time. The first order estimate $\dot{m}_{BOG} \approx \dot{Q}_{amb}/h_{fg}$ implicitly assumes that all the incoming heat contributes to phase change. Accounting for the measured energy partition reduces the corresponding energy-equivalent phase-change rate by the latent fraction, f_{lat}. This shows that, during closed-tank self-pressurization, ambient heat leak cannot be directly translated into vapor generation using a latent-heat-only approximation.

The dependence on fill level further demonstrates that liquid inventory cannot be treated as a simple scaling parameter. As the fill level increases from 25% to 68%, the ambient heat input increases from 10.2 to 13.6 W, consistent with the larger wetted area, while the fraction of that heat absorbed by the liquid increases from 60% to 85%. A larger inventory therefore provides higher thermal inertia and absorbs a larger fraction of the incoming heat through sensible heating but simultaneously increases the wetted area through which heat enters the liquid. Consequently, the storage response cannot be inferred from liquid inventory or heat leak alone: an assessment of the conditions governing vapor generation and thermal hold-time must account for their coupled variation and for the partition of the absorbed energy among the liquid, wall, and phase-change contributions.

6. Conclusions

A small-scale liquid nitrogen facility was used to investigate cryogenic chilldown and boil-off through a series of controlled experiments targeting the roles of initial thermal conditions, driving pressure, and liquid fill level. The results provide a picture of how these parameters govern transient cooling behavior, transfer efficiency, and tank self-pressurization. The measurements were reduced through a single quantitative framework combining a chilldown and transfer efficiency parameter, a transfer to cooling timescale ratio and a closed tank energy balance validated against a matched natural/forced boil-off pair. All derived quantities are reported with propagated $K = 2$ expanded uncertainties.

Table 15
Per-run partition of the closed tank first law (Eq. (28)) over the quasi-steady window. $\dot{Q}_{amb}$ is obtained as the residual through Eq. (25). Uncertainties are $K = 2$ expanded. Fractional contributions f_i are normalized by the total $P_{heater} + \dot{Q}_{amb}$.

Run	P_{heater} [W]	$\dot{Q}_{amb}$ [W]	$\dot{Q}_{liq}$ [W]	$\dot{Q}_{lat}$ [W]	$\dot{Q}_{wall}$ [W]	f_{liq} [%]	f_{lat} [%]	f_{wall} [%]
BO1	0.0	10.21 ± 0.25	6.12	1.35	2.69	60.0	13.3	26.4
BO2	0.0	11.52 ± 0.30	7.65	1.19	2.64	66.4	10.4	22.9
BO3	0.0	13.59 ± 0.42	11.52	0.28	1.78	84.8	2.0	13.1
FBO2	45.0	11.47 ± 1.96	47.82	1.17	7.44	84.7	2.1	13.2

The reference chilldown of the feed tank reproduces both the cooling-curve morphology and the quasi-steady cooling rate reported for the same facility in previous studies, supporting the reliability of the measurement chain and the consistency of the experimental methodology. Building on this baseline, the influence of the initial thermal state of the transfer system was examined by comparing pre-cooled and ambient configurations. Pre-cooling the transfer line and receiving tank then reduces the wall-enthalpy demand Q_{cd} by approximately a factor of three (CD1-tr versus CD2), increasing the delivered fraction from $\eta = 0.55$ to $\eta = 0.65$ while leaving the procedure effectiveness essentially unchanged ($\varepsilon_{tr} \approx 0.75$ in both cases). Increasing the driving pressure from ambient to 2 bar shortens the transfer duration by more than an order of magnitude but does not measurably reduce the wall enthalpy that must be removed: Q_{cd} for CD3 matches CD2 to within one percent, while the delivered fraction falls to $\eta = 0.104 \pm 0.003$ and the procedure effectiveness to $\varepsilon_{tr} = 0.13$. This reduction is accompanied by a large residual non-delivered fraction, $\eta_{res} = 0.68$, consistent with the substantially shorter transfer duration ($\Pi_t = 0.47$ versus 4.49). In CD3, transfer is therefore completed on a timescale shorter than that required for substantial progressive cooling of the receiving-side wall, leaving a larger fraction of the transferred inventory exposed to the initial wall superheat. The comparison thus shows that increasing

pressure can accelerate transfer without removing the thermal penalty associated with the initial wall state.

Boil-off behavior under closed tank conditions is dominated by sensible heating of the liquid inventory, which accounts for 60%–85% of the total energy budget across the range of fill levels investigated, while net phase change contributes only 2%–13%. The relative importance of sensible heating increases with liquid fill level, whereas the relative contributions of wall heating and phase change decrease.

The first operation of the facility's immersed electrical heater provides an independent validation of the reduction chain: the differential closure between matched forced and natural boil-off runs recovers the nominal 45 W heater input to within 5% ($\Gamma = 0.95$).

Taken together, these results establish a quantitative basis for evaluating cryogenic filling and subsequent storage response at the system level. The experiments show that transfer speed, cryogen consumption, liquid retention, and thermal conditioning are coupled rather than independently optimized, while the closed-tank measurements demonstrate that heat input cannot be equated directly with boil-off generation. Overall, the dataset offers a useful experimental reference for the analysis and validation of models describing cryogenic chilldown, two-phase flow, and tank self-pressurization, particularly in the range of conditions relevant to small-scale systems and ground-based testing of cryogenic propellants. Future work will extend the investigation of forced boil-off to higher heat fluxes and, in parallel, upgrade the instrumentation to resolve axial temperature distribution in the transfer line and increase spatial resolution within the tanks, with the aim of capturing flow-regime transitions during pressure-driven chilldown.

CRediT authorship contribution statement

Alessandra Zumbo: Conceptualization, Methodology, Investigation, Formal analysis, Data curation, Writing – original draft. **Andrea Ferrero:** Supervision, Resources, Conceptualization, Writing - review & editing. **Filippo Masseni:** Investigation, Methodology, Formal analysis, Writing - review & editing. **Dario Pastrone:** Supervision, Resources, Conceptualization, Writing - review & editing.

Declaration of competing interest

The authors declare that they have no known competing financial interests or personal relationships that could have appeared to influence the work reported in this paper.

Appendix

A.1. Simplified energy balance for boil-off experiments

The differential closure for the boil-off energy balance is derived using a homogeneous-fluid approximation. Following the homogeneous-fluid framework established by Lin et al. [50] for the analysis of cryogenic self-pressurization, and also adopted in related propellant self-pressurization problems [51], the fluid is treated as a homogeneous saturated two-phase mixture in thermal equilibrium with the tank wall. The total mass m of nitrogen and the internal volume V are both conserved throughout the run, so that the mean specific volume

$$v_m = \frac{V}{m} = \text{const} \tag{26}$$

is fixed at its initial value. The mixture state is therefore fully described by a single variable, the saturation temperature T_1, with the quality determined at every instant by the volume constraint:

$$x(T_1) = \frac{v_m - v_l(T_1)}{v_v(T_1) - v_l(T_1)} \tag{27}$$

where $v_l(T)$ and $v_v(T)$ are the saturated-liquid and saturated-vapor specific volumes obtained from NIST reference data through CoolProp.

The first law for the closed system then reads

$$P_{\text{heater}} + \dot{Q}_{\text{amb}} = m \left.\frac{du_m}{dT}\right|_{\text{sat}} \frac{dT_1}{dt} + m_w\, c_w(T_1) \frac{dT_1}{dt} \tag{28}$$

where $u_m = (1-x)\,u_l + x\,u_v$ is the mean specific internal energy of the mixture and $m_w c_w(T_1)$ accounts for the wall contribution. Expanding du_m/dT along the saturation line yields

$$\left.\frac{du_m}{dT}\right|_{\text{sat}} = (1-x) \left.\frac{du_l}{dT}\right|_{\text{sat}} + x \left.\frac{du_v}{dT}\right|_{\text{sat}} + \left(u_v - u_l\right) \frac{dx}{dT} \tag{29}$$

with the quality derivative obtained by differentiating Eq. (27):

$$\frac{dx}{dT} = -\frac{1}{v_v - v_l} \left.\frac{dv_l}{dT}\right|_{\text{sat}} - \frac{v_m - v_l}{(v_v - v_l)^2} \left(\left.\frac{dv_v}{dT}\right|_{\text{sat}} - \left.\frac{dv_l}{dT}\right|_{\text{sat}} \right) \tag{30}$$

All saturation-line derivatives in Eqs. (29)–(30) are evaluated numerically from NIST/CoolProp by central differences in T. This formulation enforces mass and volume conservation exactly, together with the saturation constraint, and reduces the energy balance to a single ordinary differential equation in T_1. The latent contribution emerges automatically as the term $m\,(u_v - u_l)\,(dx/dT)\,(dT_1/dt)$ and $du_l/dT|_{\text{sat}}$ and $du_v/dT|_{\text{sat}}$ are obtained directly from saturation-line property tables and correspond to the saturated path imposed by the closed tank mass and volume constraints. Eq. (28) is applied per run in Section 5.2 to partition the sink budget among liquid sensible, wall storage, net phase change and vapor sensible contributions, with $\dot{Q}_{\text{amb}}$ obtained as the residual.

Differential closure. The ambient heat in-leak $\dot{Q}_{\text{amb}}$ cannot be measured independently, but it can be eliminated by comparing a forced boil-off run against a natural boil-off run conducted at matched initial fill level. Writing Eq. (28) for FBO2 and BO3 and subtracting, under the assumption that $\dot{Q}_{\text{amb}}$ is the same in the two runs (matched T_1 window, identical insulation state):

$$\Gamma = \frac{\left[m \left.\frac{du_m}{dT}\right|_{\text{sat}} + m_w\, c_w(T_1) \right] \Delta\left(\frac{dT_1}{dt}\right)}{P_{\text{heater}}} \tag{31}$$

with $\Delta(\cdot) = (\cdot)_{\text{FBO2}} - (\cdot)_{\text{BO3}}$ and the bracketed coefficient evaluated at the mean temperature of the matched window. A value Γ close to unity confirms that the facility's measurement chain recovers the known heater input.

To verify the energy balance for experiments BO3 and FBO2, Eq. (31) is evaluated using the OLS-fitted slopes dT_1/dt reported in Table 12, each obtained over the quasi-steady window of its run. The differential balance evaluated on the matched FBO2/BO3 window yields $\Gamma = 0.95$, confirming that the facility recovers the nominal 45 W heater power to within 5%.

A.2. Measurement uncertainty

Uncertainties were evaluated following the Guide to the Expression of Uncertainty in Measurement [39]. The standard uncertainties $u(x_i)$ of the input quantities were combined through the law of propagation of uncertainty,

$$u_c^2(y) = \sum_i \left(\frac{\partial f}{\partial x_i} \right)^2 u^2(x_i) \tag{32}$$

and expanded with a coverage factor $K = 2$ (approximately 95% coverage). All values quoted as $\pm U$ in the paper and all shaded bands in the figures are expanded uncertainties $U = 2\,u_c$.

Type B contributions were taken from the sensor specifications, the geometric tolerances and the property data. A tolerance $\pm a$ with no stated distribution was treated as rectangular, $u = a/\sqrt{3}$. Type A contributions were evaluated from the signal noise within each run. The input quantities were defined so as to be mutually independent: an error source common to several quantities, such as the offset of a pressure cell, the tank geometry or the steel properties, was entered as

Table 16
Median expanded uncertainty U ($K = 2$) of the plotted bands.

Quantity	Unit	CD0	CD1	CD1-tr	CD2	CD3	BO1	BO2	BO3	FBO1	FBO2
T_1	K	0.36	0.35	0.35	0.36	0.37	0.36	0.36	0.36	0.36	0.37
T_2	K	0.84	0.54	0.36	0.36	0.37	0.71	0.80	0.75	0.74	0.78
T_3	K	0.84	0.57	0.57	0.70	0.71	0.71	0.75	0.72	0.69	0.72
T_4	K	0.84	0.73	0.72	0.84	0.85	0.78	0.84	0.82	0.74	0.85
T_5	K	0.85	0.52	0.39	0.42	0.45	0.70	0.84	0.80	0.69	0.84
H_f	mm	–	1.3	1.6	1.7	0.87	0.94	1.0	1.3	0.90	0.88
H_r	mm	–	0.88	0.88	0.88	0.87	–	–	–	–	–
$\dot{m}_f$	$g\,s^{-1}$	–	0.67	1.0	1.1	2.0	–	–	–	–	–
$\dot{m}_r$	$g\,s^{-1}$	–	0.009	0.042	0.020	0.022	–	–	–	–	–
Wall heat flux	$W\,m^{-2}$	20.7	2.5	–	–	–	0.42	0.41	0.28	1.2	0.97

a single input wherever it acts, so that the correlations it induces are carried by the model and no covariance terms remain in Eq. (32).

Type A uncertainties were obtained from a statistical analysis of the recorded signals. For each channel and run, the standard deviation of the measurement noise was estimated from the fluctuations of the signal about its local trend, and propagated through the smoothing and differentiation filters used in the data reduction, taking into account the correlation between consecutive samples where present.

Each derived quantity was then propagated with Eq. (32) from its defining equation. For each reported quantity, the individual contributions to the combined standard uncertainty were recorded and the adequacy of the coverage factor $K = 2$ was verified. Table 16 gives the median expanded uncertainty of each plotted band. The sensor term dominates every temperature band, so U follows the temperature: about 0.36 K near 78 K and 0.85 K near ambient. The largest values occur at the ends of the records and during fast transients.

Data availability

Data will be made available on request.

References

[1] J. Hartwig, S. Darr, A. Asencio, Assessment of existing two phase heat transfer coefficient and critical heat flux correlations for cryogenic flow boiling in pipe quenching experiments, Int. J. Heat Mass Transfer 93 (2016) 441–463, http://dx.doi.org/10.1016/j.ijheatmasstransfer.2015.09.028.

[2] R.F. Barron, G.F. Nellis, Cryogenic Heat Transfer, second ed., CRC Press, 2017, URL: https://books.google.it/books?id=_gdEDwAAQBAJ.

[3] R. Scurlock, The future with cryogenic fluid dynamics, Phys. Procedia 67 (2015) 20–26, http://dx.doi.org/10.1016/j.phpro.2015.06.005, Proceedings of the 25th International Cryogenic Engineering Conference and International Cryogenic Materials Conference 2014.

[4] A. Simonini, M. Dreyer, A. Urbano, F. Sanfedino, T. Himeno, P. Behruzi, M. Avila, J. Pinho, L. Peveroni, J.-B. Gouriet, Cryogenic propellant management in space: open challenges and perspectives, Npj Microgravity 10 (1) (2024) 34, http://dx.doi.org/10.1038/s41526-024-00377-5.

[5] W.L. Johnson, J.R. Stephens, Nasa's cryogenic fluid management technology development roadmaps, in: JANNAF in-Space Chemical Propulsion TIM, NASA, Huntsville, AL, 2018, Paper No. 20190000305, Report No. GRC-E-DAA-TN60252, URL: https://ntrs.nasa.gov/citations/20190000305.

[6] H.C. Hansen, W.L. Johnson, M. Meyer, A. Werkheiser, J.R. Stephens, Cryogenic fluid management technologies enabling for the Artemis program and beyond, in: ASCEND 2020 Proceedings, 2020, http://dx.doi.org/10.2514/6.2020-4000.

[7] J.R. Clark, On-Orbit Cryogenic Refueling: Potential Mission Benefits, Associated Orbital Mechanics, and Fuel Transfer Thermodynamic Modeling Efforts (Master's thesis), The Ohio State University, 2021, URL: https://ntrs.nasa.gov/citations/20210014171, NASA NTRS Document ID 20210014171.

[8] Z. Zuo, W. Zhu, Y. Huang, L. Wang, L. Tong, A review of cryogenic quasi-steady liquid-vapor phase change: Theories, models, and state-of-the-art applications, Int. J. Heat Mass Transfer 205 (2023) 123916, http://dx.doi.org/10.1016/j.ijheatmasstransfer.2023.123916.

[9] T. Wallner, H. Lohse-Busch, S. Gurski, M. Duoba, W. Thiel, D. Martin, T. Korn, Fuel economy and emissions evaluation of BMW hydrogen 7 mono-fuel demonstration vehicles, Int. J. Hydrog. Energy 33 (24) (2008) 7607–7618, http://dx.doi.org/10.1016/j.ijhydene.2008.08.067.

[10] M. Soleymani, V. Mostafavi, M. Hebert, S. Kelouwani, L. Boulon, Hydrogen propulsion systems for aircraft, a review on recent advances and ongoing challenges, Int. J. Hydrog. Energy 91 (2024) 137–171, http://dx.doi.org/10.1016/j.ijhydene.2024.10.131.

[11] L. Folcarelli, G. Gedda, A. Zumbo, A. Ferrero, F. Masseni, D. Pastrone, Integrated numerical modeling of a hydrogen turbofan engine and fuel system with alternative thermodynamic cycles, in: AIAA SCITECH 2025 Forum, American Institute of Aeronautics and Astronautics, 2025, http://dx.doi.org/10.2514/6.2025-0328, Paper No. 2025–0328.

[12] E.J. Adler, J.R. Martins, Hydrogen-powered aircraft: Fundamental concepts, key technologies, and environmental impacts, Prog. Aerosp. Sci. 141 (2023) 100922, http://dx.doi.org/10.1016/j.paerosci.2023.100922, Special Issue on Green Aviation.

[13] A. Sharafian, H. Talebian, P. Blomerus, O. Herrera, W. Mérida, A review of liquefied natural gas refueling station designs, Renew. Sustain. Energy Rev. 69 (2017) 503–513, http://dx.doi.org/10.1016/j.rser.2016.11.186.

[14] Y. Shirai, H. Tatsumoto, M. Shiotsu, K. Hata, H. Kobayashi, Y. Naruo, Y. Inatani, K. Kinoshita, Forced flow boiling heat transfer of liquid hydrogen for superconductor cooling, Cryogenics 51 (6) (2011) 295–299, http://dx.doi.org/10.1016/j.cryogenics.2010.05.004, Special Issue: ACASC 2009.

[15] G. Ventura, L. Risegari, The Art of Cryogenics: Low-Temperature Experimental Techniques, Elsevier, 2010.

[16] R.A. Hopkins, W.L. Chronic, Long-term cryogenic space storage system, in: K.D. Timmerhaus (Ed.), Advances in Cryogenic Engineering, Springer US, Boston, MA, 1973, pp. 486–493, http://dx.doi.org/10.1007/978-1-4684-3111-7_59.

[17] M.M. Hasan, C. Lin, N.T.V. Dresar, Self-pressurization of a flightweight liquid hydrogen storage tank subjected to low heat flux, in: ASME/AIChE National Heat Transfer Conference, no. 19910011011, NASA, 1991, URL: https://ntrs.nasa.gov/citations/19910011011.

[18] J. Joseph, G. Agrawal, D.K. Agarwal, J.C. Pisharady, S.S. Kumar, Effect of insulation thickness on pressure evolution and thermal stratification in a cryogenic tank, Appl. Therm. Eng. 111 (2017) 1629–1639, http://dx.doi.org/10.1016/J.APPLTHERMALENG.2016.07.015.

[19] T.A. Lance, R.J. Beale, A. Manager, Analysis of propellant slosh dynamics and generation of an equivalent mechanical model f o r use in preliminary voyager autopilot design studies, 1966, National Aeronautics Space Administration, URL: https://api.semanticscholar.org/CorpusID:115721574.

[20] M.E. Moran, N.B. Mcnelis, M.T. Kudlac, M.S. Haberbusch, G.A. Satomino, G.A. Satornino, Experimental results of hydrogen sloshing a 62 cubic foot (1750 liter) tank, in: 30th Joint Propulsion Conference and Exhibit, 1994, http://dx.doi.org/10.2514/6.1994-3259.

[21] J. Lacapere, B. Vieille, B. Legrand, Experimental and numerical results of sloshing with cryogenic fluids, in: EUCASS Proceedings Series, EDP Sciences, 2009, pp. 267–278, http://dx.doi.org/10.1051/eucass/200901267.

[22] Y. Qiu, H. Yang, L. Tong, L. Wang, Research progress of cryogenic materials for storage and transportation of liquid hydrogen, Metals 11 (7) (2021) http://dx.doi.org/10.3390/met11071101.

[23] S. Darr, H. Hu, N. Glikin, J. Hartwig, A. Majumdar, A. Leclair, J. Chung, An experimental study on terrestrial cryogenic transfer line chilldown I. Effect of mass flux, equilibrium quality, and inlet subcooling, Int. J. Heat Mass Transfer 103 (2016) 1225–1242, http://dx.doi.org/10.1016/j.ijheatmasstransfer.2016.05.019.

[24] S. Darr, H. Hu, N. Glikin, J. Hartwig, A. Majumdar, A. Leclair, J. Chung, An experimental study on terrestrial cryogenic tube chilldown II. Effect of flow direction with respect to gravity and new correlation set, Int. J. Heat Mass Transfer 103 (2016) 1243–1260, http://dx.doi.org/10.1016/j.ijheatmasstransfer.2016.08.044.

[25] L. Jin, C. Park, H. Cho, C. Lee, S. Jeong, Experimental investigation on chill-down process of cryogenic flow line, Cryogenics 79 (2016) 96–105, http://dx.doi.org/10.1016/j.cryogenics.2016.08.006.

[26] J. Hartwig, P. Meyerhofer, B. Stiegemeier, R. Morehead, Liquid methane and liquid oxygen horizontal chilldown experiments of a 2.54 and 11.43 cm transfer line, Appl. Therm. Eng. 205 (2022) 118042, http://dx.doi.org/10.1016/j.applthermaleng.2022.118042.

[27] J.K. Narayanan, J.W. Hartwig, J.R. Mackey, M. Kassemi, C.R. Kharangate, Experimental investigations on the flow boiling and heat transfer characteristics during chilldown process in a closed loop chilldown test section, Int. J. Heat Mass Transfer 232 (2024) 125915, http://dx.doi.org/10.1016/j.ijheatmasstransfer.2024.125915.

[28] S. Kim, N. Damle, I. Mudawar, J. Hartwig, Experimental heat transfer results and flow visualization of horizontal near-saturated liquid nitrogen flow boiling in uniformly heated circular tube under earth gravity, Appl. Therm. Eng. 246 (2024) 122934, http://dx.doi.org/10.1016/j.applthermaleng.2024.122934.

[29] D.J. Chato, R. Sanabria, Review and test of chilldown methods for space-based cryogenic tanks, in: 27th Joint Propulsion Conference Cosponsored By the AIAA, SAE, ASME, and ASEE, no. 19910016037, NASA, Lewis Research Center Cleveland, Ohio, 1991, URL: https://ntrs.nasa.gov/citations/19910016037.

[30] F. Perez, S.Z. Al Ghafri, L. Gallagher, A. Siahvashi, Y. Ryu, S. Kim, S.G. Kim, M.L. Johns, E.F. May, Measurements of boil-off gas and stratification in cryogenic liquid nitrogen with implications for the storage and transport of liquefied natural gas, Energy 222 (2021) 119853, http://dx.doi.org/10.1016/j.energy.2021.119853.

[31] G.-M. Jeon, J.-C. Park, J.-W. Kim, Y.-B. Lee, D.-S. Kim, D.-E. Kang, S.-B. Lee, S.-W. Lee, M.-C. Ryu, Experimental and numerical investigation of change in boil-off gas and thermodynamic characteristics according to filling ratio in a C-type cryogenic liquid fuel tank, Energy 255 (2022) 124530, http://dx.doi.org/10.1016/j.energy.2022.124530.

[32] Y. Kim, C. Lee, J. Park, M. Seo, S. Jeong, Experimental investigation on no-vent fill process using tetrafluoromethane (CF4), Cryogenics 74 (2016) 123–130, http://dx.doi.org/10.1016/j.cryogenics.2015.12.005, 2015 Space Cryogenics Workshop, June 24–26, 2015, Phoenix, AZ Hosted by NASA Glenn Research Center, Cleveland, OH, USA.

[33] M. Xia, W. Yuan, Q. Zhang, Y. Zheng, P. Li, J. Chen, J. Xie, Experimental and numerical analysis of the chill-down process of a large horizontal cryogenic storage tank, Appl. Therm. Eng. 234 (2023) 121246, http://dx.doi.org/10.1016/j.applthermaleng.2023.121246.

[34] M. Seo, S. Jeong, Analysis of self-pressurization phenomenon of cryogenic fluid storage tank with thermal diffusion model, Cryogenics 50 (9) (2010) 549–555, http://dx.doi.org/10.1016/j.cryogenics.2010.02.021, 2009 Space Cryogenic Workshop.

[35] M. De Salve, B. Panella, Test Facility to Study the Chill Down Phase of a Liquified Gas Flow, in: 2010 14th International Heat Transfer Conference, vol. 1, in: International Heat Transfer Conference, 2010, pp. 629–636, http://dx.doi.org/10.1115/IHTC14-23120.

[36] A. Zumbo, F.D. Carlo, C. Bertani, A. Ferrero, F. Masseni, D. Pastrone, Experimental investigation of cryogenic tank chilldown and boil-off phenomena using liquid nitrogen, in: AIAA AVIATION 2026 Forum, 2026, http://dx.doi.org/10.2514/6.2026-4576.

[37] V. Bertola, E. Cafaro, D.S. Mario, W. Millett, B. Panella, An experimental study of boiling in liquid nitrogen horizontal flow, in: Proceedings of the 11th UK Heat Transfer Conference, in: Presented at the 11th UK Heat Transfer Conference, 2009, Online.

[38] National Institute of Standards and Technology, Material properties: 304 stainless (UNS S30400), 2025, URL: https://trc.nist.gov/cryogenics/materials/304Stainless/304Stainless_rev.htm. (Accessed: 19 October 2025).

[39] Joint Committee for Guides in Metrology, Evaluation of Measurement Data — Guide to the Expression of Uncertainty in Measurement, Technical Report JCGM 100:2008, BIPM, 2008, URL: https://www.bipm.org/documents/20126/2071204/JCGM_100_2008_E.pdf, GUM 1995 with minor corrections.

[40] O.R. Burggraf, An exact solution of the inverse problem in heat conduction theory and applications, J. Heat Transf. 86 (3) (1964) 373–380, http://dx.doi.org/10.1115/1.3688700.

[41] J.A. Brennan, et al., Cooldown of Cryogenic Transfer Lines – An Experimental Report, Technical Report NBS Report 9264, National Bureau of Standards (now NIST), Washington, D.C., USA, 1966, Published November 7, 1966.

[42] F. Ghaffari-Tabrizi, J. Haemisch, D. Lindner, Reducing hydrogen boil-off losses during fuelling by pre-cooling cryogenic tank, Hydrogen 3 (2) (2022) 255–269, http://dx.doi.org/10.3390/hydrogen3020015.

[43] B.E. Okpeke, C. Ait Aider, L. Baetcke, S. Ehlers, Assessment of boil-off losses and their cost implication during liquid hydrogen tank filling with and without precooling, Energies 17 (16) (2024) 4092, http://dx.doi.org/10.3390/en17164092.

[44] G. Agrawal, D.K. Agarwal, S.S. Kumar, Mathematical modeling of cryogenic feedline chilldown process, in: Proceedings of the 22nd National and 11th International ISHMT-ASME Heat and Mass Transfer Conference December, 2013, pp. 28–31.

[45] G. Agrawal, S. Sunil Kumar, D.K. Agarwal, Pressure surge during cryogenic feedline chilldown process, J. Therm. Sci. Eng. Appl. 8 (1) (2015) 011005, http://dx.doi.org/10.1115/1.4030840.

[46] A. Kashani, D.G. Luchinskiy, E. Ponizovskaya-Devine, M. Khasin, D. Timucin, J. Sass, J. Perotti, B. Brown, Optimization of cryogenic chilldown and loading operation using SINDA/FLUINT, IOP Conf. Ser.: Mater. Sci. Eng. 101 (1) (2015) 012115, http://dx.doi.org/10.1088/1757-899X/101/1/012115.

[47] J. Hartwig, J. Styborski, J. McQuillen, E. Rame, J. Chung, Liquid hydrogen line chilldown experiments at high Reynolds numbers. Optimal chilldown methods, Int. J. Heat Mass Transfer 137 (2019) 703–713, http://dx.doi.org/10.1016/j.ijheatmasstransfer.2019.03.090.

[48] R.B. Jacobs, Liquid requirements for the cool-down of cryogenic equipment, in: K.D. Timmerhaus (Ed.), Advances in Cryogenic Engineering, Springer US, Boston, MA, 1963, pp. 529–535, http://dx.doi.org/10.1007/978-1-4757-0528-7_66.

[49] Z. Zong, Specific liquid requirement to cool down cryogenic equipment, Cryogenics 119 (2021) 103368, http://dx.doi.org/10.1016/j.cryogenics.2021.103368.

[50] C.S. Lin, N.T. Van Dresar, M.M. Hasan, Pressure control analysis of cryogenic storage systems, J. Propuls. Power 20 (3) (2004) 480–485, http://dx.doi.org/10.2514/1.10387.

[51] L. Casalino, D. Pastrone, Optimal design of hybrid rockets with self-pressurizing oxidizer, in: 42nd AIAA/ASME/SAE/ASEE Joint Propulsion Conference & Exhibit, Sacramento, CA, 2006, http://dx.doi.org/10.2514/6.2006-4501, Paper No. AIAA 2006–4501.